

**A Fast, Physically-Based Subglacial Hydrology
Model Applied to the North American Ice
Complex Over the Last Glacial Cycle**

BY

©MARK B. KAVANAGH
B.Sc (PHYSICS)

A THESIS SUBMITTED TO
SCHOOL OF GRADUATE STUDIES
IN PARTIAL FULFILMENT OF THE
REQUIREMENTS FOR THE DEGREE OF
MASTERS OF SCIENCE

DEPARTMENT OF PHYSICS AND PHYSICAL OCEANOGRAPHY
MEMORIAL UNIVERSITY OF NEWFOUNDLAND

AUGUST 20, 2012

St. John's

Newfoundland

Abstract

In this project, a physically-based basal hydrology model was created using Darcian flow to represent the flow of water in a distributed drainage system and a down gradient solver for water flow is used to simulate channelized flow of water when the conditions for channel flow is met. The Darcian flow is simulated with a robust combination of the Heun and leapfrog-trapezoidal predictor-corrector schemes. These numerical schemes are applied to a set of flux-conserving equations cast over a staggered grid with water thickness at the centres and fluxes defined at the interface. There are several parameters in the basal hydrology model that make it adaptable to various ice sheets such as the till thickness and hydraulic conductivity which will differ for various compositions of bedrock underneath different ice sheets. Since the model is meant to be ran at continental scales and for full glacial cycles, the basal water pressures are limited to ice overburden pressures, and a dynamic time-stepping is used to ensure that the maximum basal water velocity is lower than the CFL condition to help prevent any numerical instabilities.

The model is validated by creating a synthetic ice sheet and placing it over different bed topographies to test basic water flow properties and mass conservation. Model validation with the synthetic ice sheet shows that the water behaves as expected with water flowing down gradient, forming lakes in a potential well or reaching the terminus and exiting the ice sheet. Channel formation occur periodically over different sections of the ice sheet and, when sizable enough to distinguish, display an arborescent pathway that is expected of R othlisberger Channels.

Acknowledgements

Over the past few years there have been many trials, tribulations, and drawbacks. So much so that it is surprising that there is enough sanity left in me to write this body of work. Despite all the challenges, I met them head on and persevered thanks to the help and support of the many great people in my life.

First of all, I am grateful to my supervisor, Dr. Lev Tarasov, who gave me this opportunity to work on such a wonderful project (despite the aforementioned challenges). Over the last few years he has been there to offer guidance when it was needed and continually supported my project. I would also like to thank Dr. Entcho Demirov who, despite not being involved with my project, was kind enough to provide his expertise in numerical modelling to help address some of the challenges in developing the hydrology model, among other things.

I am again grateful to Dr. Tarasov and Dr. Demirov, along with Dr. Jesse Johnson, for being the reviewers of my thesis. Their insights allowed me to improve my scientific writing skills and to write the best report I could.

While working under Dr. Tarasov, I got to work with a slew of colleagues. I would like to say that it was a pleasure to work with Robert Briggs, Tristan Hauser, Kevin Le Morzadec, Alex Melanson, Taimaz Bahadory, and Andrew Keats. Each of my colleagues were a pleasure to work with providing help when need and fun and engaging conversations when they were needed more. For the same reasons as my colleagues I am grateful to wider physics community at Memorial for creating such an exciting and friendly atmosphere for me to work in.

I would like to thank all of my friends who provided just enough sanity checks to remind me how to have fun and take a break from working. If it's true that procrastination can help the brain learn and focus on work, then my friends are the best teachers to ever walk the Earth.

Lastly, I would like to thank my family. Through the best and worst times my family has always been there. My two brothers, Gordon and Jordan, and my sister Alison have always provided me with hours of enjoyment (quite often at my own expense) and their continued support is greatly appreciated. Without my parents, Albert and Joan, surely I would not be here today without their love and support (and home cooking).

Contents

Abstract	ii
Acknowledgements	iii
Table of Contents	iv
List of Tables	vii
List of Figures	viii
List of Variables	xii
1 Introduction	1
1.1 Climate Change and Sea Level Rise	1
1.2 Glaciers as Agents of Climate Change	2
1.3 Hydrology	3
1.4 Glacial Flow	5
1.4.1 Slow Flow	5
1.4.2 Fast Flow	6
1.5 The Scope of this Study	8
2 Subglacial Drainage Systems	11
2.1 Distributed Drainage System	11
2.1.1 Thin Water Film	12
2.1.2 Linked-Cavities	15
2.1.3 Braided Canals	18
2.1.4 Porous Media via Darcian Flow	19
2.2 Channelized Drainage Systems	19
2.2.1 Nye Channels	20
2.2.2 Röhrlisberger Channels	20
3 The Ice Sheet Model	25
3.1 Introduction	25
3.2 Mass Balance	26

3.3	Ice Dynamics	27
3.4	Ice Thermodynamics	28
4	Formulation of the Basal Hydrology Model	29
4.1	Discretization of the Mass Balance Equation	29
4.1.1	The Governing Equation	29
4.1.2	Expanding the Terms	30
4.2	Advancing the Mass Balance Equation in Time	31
4.3	Darcian Water Flux, \bar{Q}	34
4.4	Hydraulic Conductivity	35
4.5	Water Pressure	36
4.6	The saturated sediment parameter, h_e	39
4.7	Tunnel Flow	40
4.7.1	Theory	40
4.7.2	Implementation	42
4.8	The Source Terms	44
4.9	Flux limiting	45
5	Model Validation	47
5.1	Introduction	47
5.2	Mass Conservation and Symmetry of Darcian Flow	49
5.2.1	Study 1: Ice Sheet on a Flat Bed	50
5.2.2	Study 2: Ice Sheet on an Inclined Plane	51
5.2.3	Study 3: Ice Sheet in a Valley	53
5.2.4	Study 4: Ice Sheet Over a Dilating Bed	56
5.3	Water flow beneath the ice sheet with the inclusion of tunnels	58
5.3.1	Study 5: Ice Sheet on a Flat Bed	58
5.3.2	Study 6: Ice Sheet on an Inclined Plane	59
5.3.3	Study 7: Ice Sheet on an Inclined Plane in a Valley	61
5.3.4	Study 8: Ice Sheet Over a Dilating Bed	62
5.3.5	Study 9: Doubling the Grid Resolution	63
5.4	A quick overview of the validation results	64
6	One-way Coupling of the Hydrology Model to the GSM	66
6.1	The Baseline Model	67
6.2	Effects of Varying Parameters on Basal Water Thickness	74
6.3	Identifying Areas of Fast Flow and Esker Formation	77
6.4	Model Runtime	81
7	Conclusion	82
7.1	Summary	82
7.1.1	Summary of Model Results	84
7.2	Future Work	85

7.2.1	Examine dynamics with full 2-way coupling of hydrology model with the GSM	85
7.2.2	Examine Sensitivity to value of Exponent in the Basal Water Pressure Equation	86
7.2.3	Recast the Saturated Sediment Parameter, h_e , into a Spatially Dependent Variable	87
7.2.4	Develop a Physically-Based Aquifer	87
Bibliography		89
A One-way Coupling of the Hydrology Model to the GSM: In-Depth Analysis		97
A.1	Parameter Impacts on Basal Water Storage	97
A.2	Effects of Varying Parameters on Basal Water Distribution	101
B Discretization of the Basal Hydrology Model		117
B.1	Applying Approximations to the Mass Balance Equation	117
B.2	Discretizing the Darcian Water Flux	119
B.3	Summary of Discretized Equations Used in Hydrology Model	120
B.3.1	The Mass Balance Equation	120
B.4	The Darcy Water Flux Equation	121
B.5	Hydraulic Conductivity	122
B.6	Basal Water Pressure	122
B.7	Condition for Tunnel Formation	122

List of Tables

4.1	List of the variables used in the model description.	33
6.1	Chosen values for the baseline model run.	67

List of Figures

2.1	a) Step cavities are formed as ice undergoes regelation around a bump. b) Wave cavities are formed as ice needs time to fill-in a depression of the bed.	15
2.2	a) Aerial view of a linked-cavity system. The large open cavities are linked together by small tunnel-like connections, called orifices. b) As an orifice becomes unstable, as according to Kamb's orifice stability parameter, it can develop into a channelized drainage system. Images taken from Kamb (1987). Reproduced by permission of American Geophysical Union.	16
4.1	Variations of subglacial hydraulic conductivity K with respect to changes in hydraulic parameters k_a and k_b for values of K ranging between 1.0×10^{-7} – 1.0×10^{-5}	37
4.2	a) shows the bed topography separated into a trend and anomaly. b) The gaps in the anomalies are filled in with sediment where the hard bedrock and soft sediment make up the underlying substrate.	38
4.3	Proposed relationships for a) P with respect to A_f , b) P with respect to w , and c) analytic approximation (eqn. 4.15) to curve of $q = 10$. Image modified from Flowers (2000) with permission.	38
4.4	Hydrology model flow chart highlighting the processes involved in simulating basal water flow.	43
5.1	Final dimension of the ice dome used in model testing (for a flat topography).	48
5.2	Water Gain/Loss represented as a) maximum volume loss in cell and b) maximum water thickness discrepancy in a cell.	50
5.3	a) Basal water distribution after 20kyr run with an ice sheet resting on a flat bed, and b) the basal water pressure with arrows indicating the direction of water movement. Water moves radially away from the centre of the ice sheet perpendicular to areas of constant basal pressure according to eqn. 4.15.	51
5.4	Final set-up to test the downward flow of water.	52

5.5	a) Basal water distribution after 20kyr run with an ice sheet resting on an inclined plane, and b) the basal water pressure and flow lines showing faster flowing water on the south side of the ice sheet.	53
5.6	Final set-up to test the flow of water down a potential gradient.	54
5.7	a) Water distribution of an ice sheet in a valley that restricts the flow of water from flowing out the sides of the ice sheet. b) The corresponding basal water pressure.	54
5.8	The final setup to test the formation of lakes in potential wells underneath the ice sheet.	55
5.9	a) Water distribution showing lake formation on the south and east sides of the glaciers. b) The pressure field that acts on the basal water showing the pressure minimum located where the lakes formed and the flowlines leading water into the lakes.	57
5.10	a) Tunnel formation allows much more of the water to drain from the basal environment. b) The basal water pressure is greatly reduced due to the removal of water. The addition of the tunnel code leads to symmetry being broken from section 5.2.1.	59
5.11	a) Tunnel formation allows much more of the water to drain from the basal environment. b) The basal water pressure is greatly reduced due to the removal of water.	60
5.12	a) Tunnel formation allows the water flow much easier from the sides of the glacier to the terminus in the south. b) Basal water pressures are higher on the sides where water becomes trapped, but much lower in other parts of the ice sheet.	61
5.13	a) Basal water distribution shows the formation of larger and more numerous lakes due to the inclusion of tunnels in the Darcy model. b) The formation of tunnels converge to the lakes and all the way to the terminus at the northern dip.	62
5.14	a) Model result with resolution at 0.30° . b) Model result with resolution at 0.15°	64
6.1	Basal water profiles for a) 22 kyr BP when the total water volume is high (mean thickness: 1.0644 ± 2.8317 m, max thickness: 86.40 m), and b) 18 kyr BP after the total water volume has drained away from the base. (mean thickness: 0.6918 ± 1.3160 m, max thickness: 24.91 m.)	70
6.2	Sensitivity plot at a) 22 kyr BP and b) 18 kyr BP. Plots show that different parameters are important at different times during the glacial cycle.	71
6.3	Results with maximum $dt_{max} \approx 1$ year. Basal water thickness has a mean and standard deviation of 1.0513 ± 2.6768 m with a maximum value of 86.40 m.	75
6.4	Results with $dt_{max} \approx 10$ days. Maximum basal water thickness was 86.40 m with a mean of 1.0690 ± 2.7765 m.	75

6.5	Results with $D_r=1.00\%$. The maximum basal water thickness exceeded 99.99 m and the mean thickness increased to 1.8897 ± 4.3385 m. . . .	76
6.6	Results with the range of hydraulic conductivity $k_m = 10^{-8}-10^{-3}m/s$. With the increased hydraulic conductivity, the mean basal water thickness dropped to 0.4305 ± 1.2594 m with a maximum of 27.39 m. . . .	77
6.7	Results with $h_c=0.10$ m. While not as effective as increasing hydraulic conductivity, the lower h_c decreases the mean basal water thickness to 0.8629 ± 2.1697 m with a maximum value of 55.41 m.	78
6.8	Areas with low effective pressure indicate areas of fast flowing ice. . .	79
6.9	Location of tunnel formation as the LIS began to retreat.	80
6.10	Model simulation time over 120 kyr glacial cycle for sensitivity tests. The coloured bars represent the time the model took to complete the glacial cycle as each of the model parameters on the horizontal axis was varied across their range of values. The cyan line is the mean run time and the green lines show 1 standard deviation from the mean. . .	81
A.1	Time series plot showing how model sensitivity to varying parameters changes over time.	99
A.2	Results with $F_{CFL}=0.9$. Mean water thickness: 1.06 ± 2.72 m, maximum water thickness: 86.40 m.	101
A.3	Results with maximum $dt \approx 1$ year. Mean water thickness: 1.06 ± 2.72 m, maximum water thickness: 86.40 m.	103
A.4	Results with $dt \approx 10$ days. Mean water thickness: 1.06 ± 2.72 m, maximum water thickness: 86.40 m.	103
A.5	Results with $D_r=1.00\%$. Mean water thickness: 1.18 ± 2.18 m, maximum water thickness: 27.20 m.	104
A.6	Results with $D_r=4.00\%$. Mean water thickness: 0.37 ± 0.69 m, maximum water thickness: 14.67 m.	104
A.7	Results with $dt_{tun}=1$ month. Mean water thickness: 0.71 ± 1.32 m, maximum water thickness: 24.93 m.	106
A.8	Results with $dt_{tun}=1$ year. Mean water thickness: 0.67 ± 1.29 m, maximum water thickness: 24.12 m.	106
A.9	Results with $h_c=0.10$ m. Mean water thickness: 0.86 ± 2.17 m, maximum water thickness: 55.41 m.	107
A.10	Results with $h_c=0.10$ m. Mean water thickness: 0.5718 ± 1.31 m, maximum water thickness: 23.61 m.	107
A.11	Results with $k_a=5$. Mean water thickness: 1.07 ± 2.72 m, maximum water thickness: 86.40 m.	109
A.12	Results with $k_a=60$. Mean water thickness: 1.06 ± 2.70 m, maximum water thickness: 86.40 m.	109
A.13	Results with $k_b=0.25$. Mean water thickness: 1.07 ± 2.72 m, maximum water thickness: 86.40 m.	110

A.14 Results with $k_b=0.95$. Mean water thickness: 1.07 ± 2.72 m, maximum water thickness: 86.40 m.	110
A.15 Results with $k_m = 10^{-5}-10^{-3}m/s$. Mean water thickness: 1.01 ± 2.65 m, maximum water thickness: 85.45 m.	112
A.16 Results with $k_m = 10^{-5}-10^{-3}m/s$. Mean water thickness: 0.43 ± 1.26 m, maximum water thickness: 27.39 m.	112
A.17 Results with $Qc = 10^{-2}$. Mean water thickness: 0.44 ± 1.30 m, maximum water thickness: 27.40 m.	113
A.18 Results with $Qc = 10^2$. Mean water thickness: 0.79 ± 1.77 m, maximum water thickness: 53.65 m.	113
A.19 Results with $T_c = 0.5^\circ C$ below PMP. Mean water thickness: 1.00 ± 2.32 m, maximum water thickness: 52.59 m.	115
A.20 Results with $T_c = 3.0^\circ C$ below PMP. Mean water thickness: 1.08 ± 2.70 m, maximum water thickness: 86.40 m.	115
A.21 Results with $Z_h = 0.05m$. Mean water thickness: 0.49 ± 1.24 m, maximum water thickness: 27.44 m.	116
A.22 Results with $Z_h = 0.50m$. Mean water thickness: 0.77 ± 1.78 m, maximum water thickness: 53.65 m.	116

List of Variables

$\dot{\epsilon}$	Strain rate
$A(T)$	Arrhenius factor
$\bar{\tau}$	Shear stress
Q_d	Ice creep flux
ρ_i	Density of ice
g	Acceleration due to gravity
z_a	Ice surface elevation
v_d	Ice creep velocity
v_j	Downward flow of ice past a bump
A	Constant factor in Glen's flow law
n	Glen's flow law exponent
$\sigma_{e,j}$	Effective pressure the bump feels
l_c	The distance between to bed protrusions
β	The rate of change of pressure melting point with pressure
K_T	Thermal conductivity of ice
L	Latent heat of fusion of ice
r_j	Contact radius of bed protrusion
$S_{i,j}$	Area of an ice sheet
$S_{s,j}$	Area of ice sheet in contact with bed protrusion
P_f	Ice overburden pressure
P	Basal water pressure
w, \bar{w}	Basal water thickness
\dot{m}	Melt rate of the ice
\bar{u}	Basal water velocity
Φ	Hydraulic pressure
u_b	Basal sliding velocity
κ	Thermal diffusivity
c_h	Heat transfer coefficient
S	Cross-section area of R-channel
R_h	Hydraulic radius of a tunnel
\bar{Q}	Basal water flux
Z_h	Height of bed protrusion
K_v	Constant related to ice viscosity

p_{eff}	Basal effective pressure
Ξ	Orifice stability-melting factor
τ_s	Shear strength (yield stress)
c	Cohesive strength
μ	Coefficient of internal friction
K	Hydraulic conductivity
z_b	Bed elevation
\dot{b}	Melt rate of R-channel wall
M	Amount of surface melt that reaches the base
N	Constant related to the shape of a R-channel
n'	Manning's roughness coefficient
R	Maximum distance water will toward a tunnel
τ_b	Basal shear stress (driving stress)
PDD	Positive degree days
σ_{PDD}	Standard deviation of PDD
T_m	Mean monthly temperature
T	Temperature
RS	Surface temperature of the ice
σ_{RS}	Standard deviation of RS
a	Constant value in the Arrhenius Factor
E_a	Activation energy for ice creep
R	Universal gas law coefficient
\vec{u}	Ice velocity
E	Enhancement factor to Glen's flow law used in GSM
M_s	Net mass balance of the ice at the boundaries
c_i	Specific heat of ice
E_d	Deformational heat due to ice creep
\dot{b}_s	Englacial water source that reaches the base
\dot{b}_{sb}	Basal water source due to melting at the base
d_{wa}	Drainage down to underlying aquifer
θ	Latitudinal coordinate
ϕ	Longitudinal coordinate
r	Radius of the Earth
V	Volume element of a grid cell
Δt	Time step interval
A_f	Areal fraction of saturated sediment
K_{max}	Maximum value of hydraulic conductivity
K_{min}	Minimum value of hydraulic conductivity
k_a	Steepness of hydraulic conductivity transition
k_b	Affects when hydraulic conductivity transitions
h_c	Saturated sediment layer
α	Constant set to 5/4
C	Constant related to shape of the tunnel

f	Darcy friction factor
v_m	Opening velocity of cavity/tunnel
v_c	Closure velocity of cavity/tunnel
\bar{Q}	Mean basal water flux
H_{max}	Ice thickness at ice divide for simplified ice sheet
H_{mid}	Ice thickness midway down the simplified ice sheet
H_{min}	Ice thickness at terminus of the simplified ice sheet
d	Distance down the simplified ice sheet
r_t	Distance to the terminus of the simplified ice sheet
M_d	Basal melt rate of simplified ice sheet
M_t	Basal melt at terminus of simplified ice sheet
M_i	Basal melt at interior of melt 'ring' of the simplified ice sheet
c_r	Radial thickness of basal melt 'ring'
z_A	Amplitude of the bed topography for dilating bed
c_e	radial length of flattened section of ice
H_s	Ice thickness at the beginning of flattened ice
H_d	Ice thickness in the middle of the flattened ice
F_{CFL}	Prevents breaking CFL
V_{CFL}	CFL velocity
dt_{max}	Maximum allowable time step
D_r	Percent of water drained to aquifer
dt_{tun}	Time interval between tunnel checks
h_c	Saturated Sediment thickness
K_m	Range of hydraulic conductivity
Q_{sc}	Tunnel formation condition multiplier
T_c	Basal freezing temperature below PMP
A_s	Constant inversely proportional to bed roughness

Chapter 1

Introduction

1.1 Climate Change and Sea Level Rise

Climate change is one of the major issues society faces today. While scientists cannot be completely certain of how climate change will affect our lives, many are confident it is happening and it can potentially have some negative consequences if society does not prepare adequately. The growing concern for climate change has become more apparent with government officials from around the world meeting annually to respond to the potentially harmful impacts of climate change. World governments are now working together with scientists to help curtail climate change by trying to come to a consensus on how to socially, economically, and realistically deal with it as not to hinder the growth of developing and non-developed countries that never got to have an industrial revolution like the richer, developed countries.

One of the major risks from climate change is due to sea level rise. It is expected that the sea level will rise between 0.18-0.6 m over the next century, depending on how our society and technology evolves (IPCC, 2007). The Greenland and Antarctic ice sheets hold around 96% of the world's fresh water (Paterson, 1981), as they and

other glaciers around the world melt, they will add fresh water into the oceans. As the climate warms, the increased melting of the Greenland Ice Sheet (GIS) is expected to overpower the gains from increased precipitation. This will lead a near complete melting of the GIS, contributing approximately 7 m to sea level rise (IPCC, 2007). The impact of raising the sea level will cause the flooding of coastal areas and displacing millions of people inward to higher ground.

1.2 Glaciers as Agents of Climate Change

It has long been known that glaciers and ice sheets are good indicators of climate change, as increasing global temperatures are causing a general decrease in the extent and thickness of the overwhelming majority of glaciers worldwide, even affecting the oblateness of the Earth's surface (Nerem and Wahr, 2011).

It has come to our attention that glaciers are also agents of climate change, an effect that still needs to be determined how much it influences the climate. Glaciers are highly reflective to incoming solar radiation (i.e., ice has high albedo), meaning that as glacial areal extent is reduced, more solar radiation reaches the Earth and will contribute to more ice melting and subsequent sea level rise.

For example, there were various times in the last glacial period that the air over Greenland rapidly (over decades) warmed up by 5-10°C and then slowly cooled down, these are known as the Dansgaard-Oeschger (D-O) events (Dansgaard et al., 1993), and are believed to be caused by a increases flux of fresh water into the ocean. Preceding the D-O events were the Heinrich events (Heinrich, 1988) which are identified as layers of glaciomarine sediment covering the ocean floor. Heinrich events are believe to be caused by calving of sediment-carrying icebergs from the Laurentide Ice Sheet (LIS) into the Hudson and Cabot Straits, leading to sediment deposits on the ocean

floor (Alley, 1991; Marshall, 1996; Murray and Porter, 2001).

In one theory, Heinrich events are thought to be related to the major D-O events as the calving of the ice would have provided a source of fresh water as the ice melted in the ocean (Stewart, 2005). This influx of fresh water could have stopped the ocean circulation of the North Atlantic Deep Water by temporarily levelling the buoyancy gradient from the equator the North Atlantic. This would have caused the ocean to become unstable (once the effects of the fresh water wore off) and the ocean currents rebounded with a shock that created a strong current that brought a lot of warm water to the North Atlantic, causing the air to warm up (Evatt et al., 2009).

1.3 Hydrology

Hydrology has been a study of mankind for thousands of years and has helped many civilizations grow and prosper in profound ways, such as the damming of the Nile by the Egyptians in 4000 B.C to help agriculture to flourish on once barren lands. Over time, much like many human endeavours, hydrology has grown into many subdivisions. They include: chemical hydrology, ecohydrology, hydrogeology, hydroinformatics, hydrometeorology, isotope hydrology, and surface hydrology. Each of these branches of hydrology deals with different important aspects of water. For example, Chemical hydrology deals with water quality and classifies water in such groups as drinking water, irrigation water, and industrial use water and tests such parameters of the water such as its acidity and electrical conductivity. Some of the more important branches for studying glaciology are surface hydrology and hydrogeology (often called groundwater hydrology by glaciologists).

Surface hydrology deals with the flow of water in rivers, canals, lakes, and such. It is important in studying the hydrological cycle and its implications for the water

balance of an area. It deals with predicting floods and the effects of dams and culverts. It can be used to determine an adequate reservoir supply for a town in case of a drought. More specific to glaciers, it deals with the flow of water along the surface where it can form lakes and rivers on the surface, reach the terminus of the glacier and leave as glacial run-off, or it can find its way to cracks in the ice, such as crevasses and moulins. From the crevasses and moulins, the water can enter the interior of the glacier, where it can refreeze and increase ice fracturing, or it can once more reach the terminus of the glacier and leave as glacial run-off. Also, the water can continue to find its way to the base of the glacier and alter the hydrological landscape at the base of the glacier.

Groundwater hydrology is used extensively in planning that involves groundwater and aquifers. The principles of physical hydrology allow planners to determine if the waste from a manufacturing site will enter into the groundwater and reach the town's water supply. In the context of glaciers, groundwater hydrology is used, in part, to determine the dynamics of hydrological processes beneath the ice as water can flow in the pore space of the underlying till and aquifer. The inclusion of aquifers allows water trapped at the base of the ice to drain away from the ice or possibly re-emerge at a different location beneath the ice sheet (Flowers, 2000; Lemieux et al., 2008).

Groundwater hydrology, aside from modelling subglacial aquifers, can be used to simplify the modelling of an ice sheet's basal hydrology system. Basal hydrology can have major impacts on ice sheet dynamics as it can affect basal sliding (explained below). Basal sliding can lead to ice streaming which can cause calving of the ice at the terminus as the ice behind it pushes against it. It can also affect the advance and retreat of the grounding line between the ice sheet and ice shelf. Since the grounding line is where the ice begins to float in water, then its location is a function of ice thickness. This makes the problem of locating the grounding line nonlinear because

the its location is needed to know the ice thickness (Weertman, 1974). The ice thickness at the grounding line will depend on the accumulation/ablation and the influx of ice from the ice sheet. Since the influx of ice depends basal sliding, then it depends on basal hydrology as it either directly or indirectly affects basal sliding.

1.4 Glacial Flow

1.4.1 Slow Flow

The slow, or normal, flow of ice sheets is caused by the deformation of polycrystalline ice, called ice creep. In creep, the deformation of ice comes from the ice crystals being under constant stress from the weight of the ice above it. This constant application of stress, even though under the yield strength of ice, still manages to cause the ice crystals to fail and deform. Ice creep is a relatively well known process studied by Glen (1955), in his paper Glen defines an equation for ice creep as

$$\dot{\epsilon} = A(T)\bar{\tau}^n \quad (1.1)$$

which relates the shear stress $\bar{\tau}$ to the strain rate $\dot{\epsilon}$ with constants n and temperature-dependent constant $A(T)$. The Constant $A(T)$ is known as the Arrhenius factor, and $n = 3$ is known as the Glen's Flow Law exponent. Assuming that the horizontal length scales of the ice are much greater than the vertical length scales, then the shallow ice approximation From Huybrechts (1992) gives the flux, \bar{Q} , of ice from creep as

$$\bar{Q}_d = -2(\rho_i g)^3 (\bar{\nabla} z_s \cdot \bar{\nabla} z_s) \bar{\nabla} z_s \int_0^{z_s} \int_0^z A(T)(z_s - z) dz' dz \quad (1.2)$$

where $\rho_i = 910 \text{ kg/m}^3$ is the density of ice, $g = 9.81 \text{ m/s}^2$ is the acceleration due to gravity, and z_s is the height of the glacier surface. Solving the integral gives

$$\bar{Q}_d = \frac{-2(\rho_i g)^3 A(T) z_s^5}{5} (\bar{\nabla} z_s)^5 \quad (1.3)$$

to which the velocity of ice creep is given by Q_d/z_s

$$\bar{v}_d = \frac{-2(\rho_i g)^3 A(T) z_s^4}{5} (\bar{\nabla} z_s)^5 \quad (1.4)$$

for glaciers undergoing slow flow by creep the typical values for the creep velocity is $v_d = 1\text{--}10 \text{ m/year}$ (Johnson, 2002).

1.4.2 Fast Flow

Under certain conditions, some glaciers can flow with velocities well in excess of the velocities obtained by creep. For example, Kuannersuit Glacier ($69^\circ 46' \text{N}, 53^\circ 15' \text{W}$) in Greenland underwent a glacial surge (extreme fast flow) in 1995 where its velocity in the beginning of the surge 70 m/day From September 24^{th} to October 12^{th} . In 1996 and 1997 its velocity was 18 m/day and 5 m/day respectively (Fowler and Larsen, 2010). In this case, the glacier underwent a glacial surge with ice velocities in excess of 1000 m/year . Another example is Variegated Glacier, Alaska, where the surging velocity of the glacier ($\approx 10 \text{ m/d}$) was almost completely (97%) due to basal sliding (Kamb et al., 1985, 1994). These two examples show the relative importance of basal sliding in glaciers and ice streams that experience fast flowing. Typical velocities for fast flowing ice tend to be $100\text{--}200 \text{ m/year}$ (Johnson, 2002).

Fast flow is associated with instabilities in the current condition of the base of the glacier. One such instability could be caused by the deformation of the underlying

till. Since the friction between the underlying till and the ice helps restrain the ice from flowing, when the till breaks down and deforms, there is less friction to hold the ice back and it can flow down the gradient at a much faster pace than normal. The deformation of the till can be aided by the presence of basal water. If water is present in the till, then the water pressure acting on the till can weaken the cohesion of the till, which allows it to deform under less basal stresses than without the water present. One well-known example of till deformation sliding is Breiðamerkurjökull in the Vatnajökull Ice Cap, Iceland. 80-90% of Breiðamerkurjökull’s basal sliding motion is due to a deforming till layer approximately 0.5 m thick (Boulton and Jones, 1979; Benn and Evans, 2010).

The second instability has to do with subglacial hydrological processes. As will be explained in greater detail later in section 2, there are two basic types of water storage beneath an ice sheet—distributed and channelized. In a channelized system, a drainage basin of the ice sheet can be drained by a few main drainage centres, such as a conduit, that the water flows into and is quickly drained from beneath the ice. Thus channelized systems are associated with slow flowing ice. However, in the distributed system, such as thin film of water between the ice and the underlying material, there is no centre for drainage and the water does not drain efficiently from beneath the ice. When the water builds up in the distributed system, it causes the bed to become lubricated, reducing friction. As water builds up, it exerts greater pressure back up onto the ice, reducing its apparent weight. This also reduces friction and increases the sliding velocity of the overlying ice. Basal sliding is captured in numerical modelling via a “basal sliding law”, such as

$$\bar{u}_b = A_s \frac{\bar{\tau}_b^n}{P_{eff}^y} \quad (1.5)$$

where u_b is the basal sliding velocity, A_s is a constant inversely proportional to the bed roughness, $\bar{\tau}_b$ is the basal shear stress, p_{eff} is the effective pressure, p and q are parameters to be determined.

1.5 The Scope of this Study

The aim of the study is to develop a deterministic, physically-based subglacial hydrological model to be used in determining the basal sliding and till deformation at the base of the ice. The importance of these processes is that it allows the ice to move with speeds well in excess of normal glacial flow, as mention in section 1.4. The hydrology model developed in this project is heavily derived from the works of Flowers (2000), Johnson (2002), Arnold and Sharp (2002), and Schoof (2010).

Flowers (2000) developed a physically-based, multi-component model that included englacial, subglacial, and groundwater (aquifer) hydrology. Flowers's model was developed to study Trapridge Glacier, Canada on a 40x40 m Cartesian grid as discussed in much greater detail in chapter 4. This model simulates water flow at the ice-bed interface via Darcy flow (see section 2.1.4). The underlying aquifer uses Darcy flow to move water and exchange with the ice-bed interface was governed by the differences in the water pressures of the aquifer and ice-bed interface. The model solves the equations of water motion discretized in Crank-Nicolson notation (Patankar, 1980) and cast over a staggered grid. The model time steps are advanced using an iterative, Newton-Krylov technique until convergence is reached.

The work of Johnson (2002) develops a basal hydrology model to study the Ross Ice Streams. The model employs a semi-implicit variable discretization (Hindmarsh and Payne, 1996) cast over a finite-element grid with a resolution of approximately 5 km on a Cartesian grid. The water is transported using the turbulent Manning

pipe flow law. This model does not include a physically-based aquifer, but uses a parameter that drains a percentage of the water into the aquifer.

Arnold and Sharp (2002) studies the Scandinavian Ice Sheet using a continental-scale basal hydrology model. The model simulates a linked-cavity distributed drainage system using the work of Fowler (1987). The cavity system is able to become unstable and grow into a channelized system once certain conditions are met (more details in section 2.1.2). The approach of this model is to integrate the basal water fluxes down the hydraulic potential. From the fluxes, the model determines the drainage system present, which is a different method employed from those used in the previous two models and the one developed in this project. However, this model is done on continental-scale resolution of 40 km and provides a solid framework from which future models can be built upon.

The basal hydrology model described here is an attempt to combine the features of the previous models to create a hydrology model for continental-scale modelling. Following the work of Arnold and Sharp (2002), the basal drainage system is allowed to have both distributed and channelized drainage systems with a condition for determining which basal system is present. While conceptually similar, the implementation is rather different. In this model the drainage system is initially assumed to be distributed, as in Flowers (2000), and the basal fluxes are determined from the distributed drainage system. The condition for switching to a channelized drainage system is developed in Schoof (2010). From the cells that meet the switching condition, Channelized systems are created by following the path of steepest hydraulic gradient until no more paths can be created (Tarasov and Peltier, 2006). As a way to isolate the properties of the basal drainage systems, the aquifer physics of Flowers (2000) are replaced with the drainage parameter from Johnson (2002).

One of the distinguishing features of this model is the numerical time stepping

scheme. The model uses a combination of Heun's method and the leapfrog-trapezoidal schemes, which are iterative predictor-corrector schemes that will be explained in much greater detail in section 4.2. Suffice to say, the combination of these two methods prove to be robust and stable with quick convergence to the final solution.

The hydrological model is incorporated into the MUN/UoT Glacial System Model (Tarasov and Peltier, 1999; Tarasov et al., 2012). Currently till deformation and basal sliding, two of the leading causes of glacial fast flow, are parameterized. While the hydrological model will not remove parameterization, as it will have some parameterization of its own, the model will be able to better restrict the parameter set for basal sliding and allow for more glacial variability such as the switching between fast and slow flow regimes. Also, by incorporating a realistic hydrological model, changes in the glacier basal hydrology dynamics and how it interacts with other components of the model may occur. Lastly, this project will do some sensitivity testing of several hydrological parameters by using the North American Ice Complex (NAIC), which is composed of the Laurentide and Cordillera ice sheets, as a testing ground.

Chapter 2

Subglacial Drainage Systems

The focus of this chapter is to discuss various subglacial drainage systems that store and drain basal water. The cause of switching between fast and slow ice flow regimes is due to changes in the basal water pressures. Basal water pressure depends on the type of water storage beneath the ice. There are many different ways water can be stored at the base of the ice (Alley, 1996; Björnsson, 1998; Fountain and Walder, 1998), but they can be categorized into two main types: distributed and channelized.

2.1 Distributed Drainage System

A distributed drainage system is characterized by basal water being spread out over a drainage basin of an ice sheet, as opposed to water being concentrated into a small, localized system (on the order of metres). This type of drainage system tends to be poor at draining the water, allowing water pressure to build up at the base of the ice. As the water pressure builds up in a distributed drainage system, it decreases friction between the bed and the ice, leading to faster glacial sliding. The build up of water also hides the smaller, rougher elements of the bed from the ice, effectively smoothing the bed. This increases the deviatoric stress of the upstream part of the

remaining bed elements, which allows the ice to flow faster due to enhanced ice creep around these obstacles (Weertman and Birchfield, 1983a). For this reason, distributed drainage systems are associated with fast flowing ice.

There are several ways that water can be distributed underneath the ice. Water can be stored via a thin film (Weertman, 1972), linked-cavity system (Kamb et al., 1985), braided canals (Clark and Walder, 1994), and flow through a porous medium via Darcian flow (Flowers, 2000).

2.1.1 Thin Water Film

The sheet flow theory (Weertman, 1972; Lliboutry, 1987) is based on the flow of water between two plates, where the dimensionless Reynolds number is used to determine if the flow is laminar or turbulent. In this theory the ice and the bed are completely separated by the water film (essentially the ice is floating on the water film). This flow is modified due to small asperities (bumps) in the bed. Due to the bumps in the bed, the ice on the upstream side of the bump undergoes regelation and enhanced sliding, which creates more water on the downstream side of the bump that may refreeze or join the already existing water film.

However Walder (1982); Alley (1989); Clark and Walder (1994) did perturbation analyses on the water film using a perturbed planar bed and a perturbed sliding velocity and came to the conclusion that a water film of a few mm's (1-4 mm) would lead to unsteady growth. In the analysis, Walder (1982) concludes that water films are unlikely to initiate surges, but once a surge starts a water film may be able to prolong the surge.

Creyts and Schoof (2009) modified the original theory of Weertman to include bumps in the bed that the ice can partially rest on, instead of floating on the water film. In the analysis of Creyts and Schoof (2009), the bed is covered with protrusions

(bumps) of different sizes and different spatial separations, which each class of bumps indexed by the letter j . Creyts and Schoof (2009) show that when there are low hydraulic gradients, the downward flow of ice toward the bed is given by

$$v_j = A|\sigma_{e,j}|^{n-1}\sigma_{e,j}l_{e,j} + \frac{\beta K_T}{\rho_i L r_j} \frac{S_{i,j}}{S_{s,j}} \sigma_{e,j} \quad (2.1)$$

where v_j is the downward flow of ice past a bump (the closure velocity), A and n are the factors in Glen's flow law (Paterson, 1981), $\sigma_{e,j}$ is the effective pressure the bump feels, $l_{e,j}$ is the spatial separation of the bumps of that class, β is rate of change of the pressure melting point with pressure, K_T is the thermal conductivity of ice, ρ_i is the density of ice, L is the latent heat of fusion of ice, r_j is the contact radius of the bump to the ice, $S_{i,j}/S_{s,j}$ is the inverse of the fraction of the ice in contact with the bumps of class j . The first term of the right hand side is the closure due to ice creep from Glen's flow law (Glen, 1955). The second term is the closure due to regelation past the bumps. Eqn. 2.1 shows that the closure velocity of ice (preventing unstable growth) is proportional to the effective pressure due to increases of the ice creep velocity. The closure velocity is also proportional to the water film thickness since increasing the water film would drown out some of the smaller classes of bumps. This would lead to a decrease in contact area, increasing the regelation velocity. The sum of the effective pressures over all the bumps must add to give the overall effective pressure, as defined by

$$\sum \sigma_{e,j} = P_j - P \quad (2.2)$$

where P_j is the ice overburden pressure, and P is the basal water pressure. This will result in the ice creep velocity increasing with thicker water film due to the increased pressure on the larger bumps remaining in contact with the ice, which are spaced further apart than the smaller bumps.

The melting of the ice due to heating from the water film is given by

$$\frac{\partial \bar{w}}{\partial t} = \frac{\dot{m}}{\rho_w} \quad (2.3)$$

where \bar{w} is the water film thickness, \dot{m} is the melt rate of ice, and ρ_w is the density of water. The balance between the melting of the ice and the closure velocity of the ice will determine whether the thin film becomes unstable or not. Under the conditions of the model of (Creys and Schoof, 2009), this will result in the water film having multiple steady states that do not form into channelized flow (see fig. 9 from Creys and Schoof (2009)).

The 1-D analysis of Creys and Schoof (2009) works under the condition

$$\frac{3t_e|\bar{u}|\bar{\nabla}\Phi|}{2\rho_w L u_b [1 + \kappa \bar{w} 4\pi^2 / (c_h t_e^2)]} \ll 1 \quad (2.4)$$

where \bar{u} is the basal water velocity, $\bar{\nabla}\Phi$ is the hydraulic gradient, u_b is the basal sliding velocity, κ is the turbulent diffusivity, and c_h is the heat transfer coefficient. They show that water films can be stable when the hydraulic gradient is low and sliding velocities are high. They argue that under these conditions the turbulent heat diffusion may be strong enough to stop the unstable growth of the film into a channelized flow if there are protrusions located below a critical distance apart that depends on the water thickness, turbulent diffusivity, and the heat transfer coefficient between the ice and the water. In their model, the water film was able to become up to $\bar{w} \approx 3$ cm thick, but with high potential gradients the assumptions in this model breakdown and the water film behaves like the film from Weertman (1972).

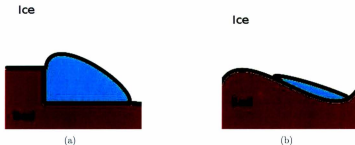


Figure 2.1: a) Step cavities are formed as ice undergoes regelation around a bump. b) Wave cavities are formed as ice needs time to fill-in a depression of the bed.

2.1.2 Linked-Cavities

Linked-Cavities (Kamb et al., 1985; Walder, 1986; Fowler, 1987) are a distributed system of gaps in the ice-bed interface. There are two ways that cavities are formed at the ice-bed interface. In the first method, called the step cavity by Kamb, ice flows past a perturbation in the bed rock undergoing regelation melting on the high pressure side of the rock and refreezing on the low pressure, leeward side of the rock (Nye, 1967). Since the ice is moving, when the water refreezes back onto the ice it would have moved away from the rock, leaving a gap between the rock and the ice. The second type of cavity formation, called a wave cavity, is formed from a bed that has a wave-like (undulating) topography. In this method, the ice rests on top of the crest of the wavy bedrock, and sags into the troughs of the bedrock. Since it takes time for ice to sag down into a trough, if the ice is flowing then there will be a gap on the leeward sides of the crests leading into the troughs.

The cavities are connected by little tunnels, called orifices, that allow water to quickly flow from one cavity to another until it reaches a dead end or flows out of the subglacial environment. The cavity system is kept open by ice moving along the bed

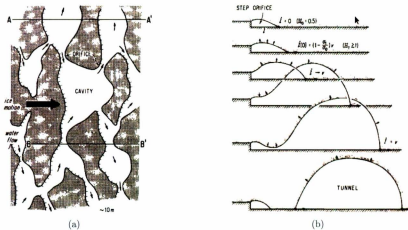


Figure 2.2: a) Aerial view of a linked-cavity system. The large open cavities are linked together by small tunnel-like connections, called orifices. b) As an orifice becomes unstable, as according to Kamb's orifice stability parameter, it can develop into a channelized drainage system. Images taken from Kamb (1987). Reproduced by permission of American Geophysical Union.

(as mentioned previously), and by water pressure pushing on the sides of the cavity wall. Also, when the water is moving (more so in the orifices than the cavities), it causes viscous heating of the walls and expands the size of the cavity/orifice. The cavities and orifices close when the water present is no longer able to resist closure due to ice creep and refreezing. This can be represented as

$$\frac{\partial S}{\partial t} = \frac{1}{\rho_w L} |\bar{Q}| \bar{\nabla} \Phi + |\bar{u}_b| Z_h - K_\nu p_{eff} S \quad (2.5)$$

where S is the cross-sectional area of the cavity, Z_h is the cavity step height (bumps at the bed), $K_\nu = 2An^{-n}$ is a constant related to ice viscosity, $p_{eff} = P_I - P$ is the basal effective pressure with P_I representing the ice overburden pressure and P is the basal water pressure.

In Kamb's model (Kamb et al., 1985; Fowler, 1987), the cavities are treated as relatively stable features and the variations in orifice geometry are the main consideration. The geometry of the orifice changes due to opening from viscous heating caused by water flow and closure due ice deformation. Kamb et al. (1985) define a "orifice melting-stability factor", Ξ , that relates the importance of viscous melting of the orifice roof in comparison to roof closure from the overburden ice pressure. When $\Xi > 1$, the orifice can become unstable and grow without bound. Kamb reasons that the unbounded growth can be physically explained as the dominant drainage system underneath the ice sheet switching from a distributed linked-cavity system to a centralized tunnel system. This switch from linked-cavity to channelized flow causes a surging ice stream to quickly drain its stored water and to stop surging.

The study of cavities in the field uses dye tracers to identify the system underneath the ice. To study the properties of cavities requires drilling boreholes down into the cavity. On deglaciated beds, cavities are often identified as areas of the bed that show

little erosion as the ice would not have much contact with the bed where water-filled cavities existed (Walder and Hallet, 1979).

2.1.3 Braided Canals

Clark and Walder (1994) introduces the concept of the braided canal as a pathway for high pressure water to flow that is cut into the sediment. Clark and Walder (1994) compares R-channels (tunnels incised upward into ice, discussed in section 2.2.2) to canals incised into the substrate (not to be confused with Nye channels discussed in section 2.2.1). A canal is formed when high pressure water along with a shallow slope causes the underlying sediment to break under the shear stresses. The till will break when the shear stress exceeds the substrate's shear strength given by

$$\tau_s = c + \mu p_{eff} \tag{2.6}$$

with c as the cohesive strength, μ as the coefficient of internal friction (also described in Paterson (1981)).

In the theory by Walder and Fowler (1994), the effective pressure of the canal is inversely proportional to the flux ($p_{eff} \propto |\vec{Q}|^{-1/n}$). This means, like the cavities and unlike the R-channels, there is no tendency for canals to capture water from each other since increasing the flux will increase the water pressure. This will prevent water from gathering into a single canal (since water will flow away from high pressures), and they can form a distributed drainage system. The formation of canals also depends on the type of till present. Canals will unlikely form in hard bedrock or sandy tills due to such substrates having better cohesion and more pore space to help keep the water pressure low. Canals are more likely to form in tills that are more fine-grained, clay-like due to weaker cohesion and less pore space to store water.

2.1.4 Porous Media via Darcian Flow

The idea of using Darcian flow is borrowed from the older science of groundwater flow through aquifers. In this type of model the water flux is given by the Darcy flow equation

$$\vec{Q} = \frac{Kw}{\rho_w g} \vec{\nabla} \Phi \quad (2.7)$$

where K is the hydraulic conductivity, w is the water thickness $\Phi = P + \rho_w g z_b$ is the hydraulic pressure, and z_b is the bedrock topography. With the exception of braided canals, all the previous morphologies were developed for hard bed rock and not for bed rock with till. It is unlikely that the ice will be underlain by all hard bedrock since it will erode the bedrock as it moves. Also, the ice can entrain rocks and sediments to further erode the bed and move the till around.

In this system the water flows in the gaps between the underlying till and the ice (not to be confused with any groundwater flow in an underlying aquifer). Water can flow more easily through rockier substrate than clay-like substrate due to the larger pore space between the rocks. As the water becomes more pressurized (from the ice above and stockpiling of water in one location), it pushes the substrate further apart, increasing its porosity and hydraulic conductivity (Flowers, 2000; Flowers and Clarke, 2002). As the water flows faster, it can melt the ice due to frictional heating and an unstable growth of water velocity from increased water pressure and a continuous supply can lead to tunnel formation, much like the unstable growth of the linked-cavity system in section 2.1.2 (Flowers et al., 2004)

2.2 Channelized Drainage Systems

The channelized drainage system is, to a certain degree, the opposite of the distributed drainage system. This system has a lot of water concentrated in a small area of the

glacial bed, and acts to transport the water quickly from one place to another. Since channelized systems are efficient drainers of water, they tend to cause the water pressure to decrease and increase basal friction between the ice and the bed. Thus, channelized systems are associated slow flowing ice regimes. Bartholomew et al. (2011) points out that the sliding velocities near the margins of the Greenland Ice Sheet are lower in the late summer than earlier in the summer, possibly as an indication of a switch from a distributed to a channelized drainage system. There are two types of channelized drainage systems: Nye Channels that are incised down into the substrate, and R-channels that are tunnels incised up into the ice.

2.2.1 Nye Channels

Nye channels (N-Channels) are like the braided canals discussed in section 2.1.3, however they are cut into the bed rock and not sediment. This can make them a much more permanent feature than canals as sediments can become deformed and destroy the canals. N-channels can play a major role in the drainage of water since they can allow a relatively open path for the water to drain, and unlike R-channels, there is no tendency for water to flow away from N-channels (Weertman, 1972). N-channels are also more stable than R-channels, but would still likely require a source of surface melt water to remain open for a long period of time (Alley, 1989).

The study of deglaciated beds show that N-channels are long and narrow depressions in the bed. They do not form an arborescent network like R-channels, but they do tend to flow (close to) parallel the flow of ice (Walder and Hallet, 1979).

2.2.2 Röthlisberger Channels

Also known as R-channels, these are tunnels incised upward into the ice. They are formed when the rate of opening of ice from frictional melting exceeds the rate of clo-

sure due to ice deformation crushing the tunnel. This happens when there is an unstable growth of frictional melting and water formation in the distributed systems mentioned in section 2.1. A set of conservation and empirical equations (Röthlisberger, 1972; Nye, 1976; Fowler, 1987) :

$$\frac{\partial S}{\partial t} = \frac{\dot{b}}{\rho_w} - K_v S p_{eff}^2 \quad (2.8)$$

$$\frac{\partial S}{\partial t} = \frac{\dot{b}}{\rho_w} - \frac{\partial \bar{Q}}{\partial x} + M \quad (2.9)$$

$$\frac{\partial P}{\partial x} = -\rho_w g \bar{\nabla} z_b + \frac{\bar{N} Q^2}{S^{8/3}} \quad (2.10)$$

$$\frac{\partial P}{\partial x} = -\rho_w g \bar{\nabla} z_b + \frac{\dot{b} L}{|\bar{Q}|} \quad (2.11)$$

can be used to derive the relationships between basal water pressure, P ; the water flux, \bar{Q} ; and the cross-sectional area of the tunnel, S . Here \dot{b} is the mass of ice melted per unit length along the tunnel, M is the amount of surface melt water that reaches the tunnel, $\bar{\nabla} z_b$ is the slope of the bed, and L is the latent heat of fusion of ice. N is a constant as long as the shape of the tunnel does not change over time (e.g., always semi-circular), given by

$$\bar{N} = \left(\frac{S}{R_h^2} \right)^{3/2} \rho_w g n'^2 \quad (2.12)$$

where R_h , is the hydraulic radius of the tunnel, and n' is Manning's roughness coefficient.

Eqn. 2.8 describes the opening and closing of the tunnel as a balance between opening due to melting of the walls (first term on right hand side) and closure due to ice deformation trying to close the tunnel (second term on the right hand side). Eqn. 2.9 is the mass balance equation for water flowing in the tunnel. Equations 2.8 and 2.9 are related due to ice melting due to heating of the ice. As the basal ice melts there will be more water in the tunnel to push on the walls of the tunnel, forcing the

size of the tunnel to increase. Likewise water discharge will increase while tunnels are shrinking (e.g., from ice creep). Equations 2.8 and 2.9 are written with the rate of tunnel area growth/shrinkage to emphasize the relationship between the amount of water in a tunnel (eqn. 2.9) and its ability to remain open (eqn. 2.8).

Eqn. 2.10 is based on the empirical Gauckler-Manning formula described in Williams (1970), relating how the water pressure in the tunnel is related to the water flux. Lastly, eqn. 2.11 is the change of the internal energy of the tunnel. This expression relates how the melting of the ice, \dot{b} , is related to the water flux and the hydraulic potential ($\partial P_w / \partial x + \rho_w g \vec{\nabla} z$). When combined, they give

$$\dot{b} = \frac{\bar{N}}{L} \frac{|\vec{Q}|^3}{S^{8/3}} \quad (2.13)$$

which shows how the melting of the ice wall is strongly dependent on the amount of water flux and the size of the tunnel.

Using dimensional analysis Fowler (1987), with typical glacier thickness $d = 100$ m, typical tunnel length $l = 10$ km, and bed slope $\vec{\nabla} z_b = 0.1$, uses these approximations to simplify the above equations. Since $P \leq P_I$ then Fowler determines that

$$p_{eff} = P_I - P = \left[\frac{(\rho_w g \vec{\nabla} z_b)^{11/8}}{\rho_l K_\nu L \bar{N}^{3/8}} \right]^{1/8} |\vec{Q}|^{1/4n} \quad (2.14)$$

This analysis shows, from eqn. 2.14, that the water pressure is negatively correlated to the water flux; as flux increases, the water pressure in the R-Channel decreases. This means that when two R-channels meet, the larger of the two tunnels will sap water from the smaller tunnel, and form an arborescent drainage system much like regular river systems. When the tunnel loses its source of water (e.g., surface melt), the water pressure in the tunnel will decrease and the water flux in the tunnel will decrease due to lack of water. This causes the melting of the walls to decrease due to

the lack of frictional melting from water flow. These factors lead to the closure term from eqn. 2.8 to become greater than the melting term and the tunnel collapses due to ice creep deformation.

Equations 2.8-2.14 are derived for the steady case scenario. Considering that tunnels will not always have a continuous influx of water, it becomes reasonable that the tunnel will not always be full. This means that instead of being semi-circular, R-channels could be more flattened at the top where there is no water to resist the downward ice creep, and would be wider at the base and sides where the water flows. In this case, it is more likely that R-channels are broad, shallow canals incised upward into the ice instead of a semi-circular incision (Fountain and Walder, 1998; Carter et al., 2009).

Being efficient movers of large amounts of water underneath the ice, R-channels are associated with large excavations of water from the ice and flooding the nearby lands. These rapid releases of water, called Jökulhlaups, pose serious risks to those living nearby as the floods can cause serious damage to roads, buildings, and to people and livestock. An extreme case of flooding was the Pleistocene Missoula floods which swept across Washington state, creating what is known as the Scablands (Fountain and Walder, 1998).

Weertman (1972) and Weertman and Birchfield (1983b) show that, even though they are good drainage sites, they are poor water collectors and therefore most of the drainage must occur in broad thin films of water beneath the ice (or some other system). To prove this he considers the work done by pressurized water flow. To a first order approximation the pressure gradient, $\vec{\nabla}P$, is $\rho g \vec{\nabla}z_s$ and the basal stress, $\vec{\tau}_b$, is $\rho g H \vec{\nabla}z_s$, with $\vec{\nabla}z_s$ and H being the ice surface slope and ice thickness, respectively. Then, making the general assumption that R-channels are formed when sheet flow becomes unstable, if the basal stress is large compared to the pressure gradient, as

would become the case in R-channels, the water drains and there is an increase of friction (basal stress, $\bar{\tau}_b$) between the ice and underlying rock. His analysis gives that

$$2R = d(\bar{\nabla}P/\bar{\tau}_b)^n/2 \quad (2.15)$$

where R is the maximum distance from the tunnel centre that water will flow to the tunnel. This equation shows that increasing the basal stress will reduce R and thus tunnels will become poor gatherers of water. Walder and Fowler (1994) argues that this may not be the case as the analysis used straight, parallel R-channels, whereas in reality R-channels can intersect each other, and an underlying aquifer could provide an alternative route to allow water to reach the R-channels.

Studying eskers offers a paleo record of past R-channel locations from deglaciated ice sheets, like the Laurentide ice sheet (Brennand, 2000). Eskers are thought to be the sediment-filled remains of old R-channels that stayed open year-round as the ice sheets began to retreat. The R-channels would transport the sediment toward the mouth of the tunnel, depositing sediments and other materials to form eskers, possibly with the help of surface melt water (Hooke and Fastook, 2007). Since eskers typically form on hard bedrock (e.g., The Canadian Shield) and not on softer sedimentary rock, it is believed that on softer substrate, the basal water may prefer to cut into the bed as a distributed system, possibly a canal system (Boulton et al., 2007; Clark and Walder, 1994). This provides a possible explanation why there are many esker sites on the Canadian Shield, which is underlain by hard rock, and the (nearly) esker-free Canadian Prairies, which are underlain by soft sediment.

Chapter 3

The Ice Sheet Model

3.1 Introduction

The ice sheet model used in this study is based the MUN/UoT Glacial Systems Model (Tarasov and Peltier, 1999, 2002, 2004; Tarasov et al., 2012), hereafter simply referred to as GSM.

The original GSM (Tarasov and Peltier, 1997) used a 2-D, vertically integrated ice dynamics component that describes the deformation and movement of the ice due to the stresses on the ice. The GSM also employed bedrock dynamics which dealt with the isostatic sinking and rebounding of the bedrock due to the weight of the ice applying pressure to the Earth's mantle.

The model was improved in Tarasov and Peltier (1999) to include a coupled 3-D thermomechanical ice sheet component into the model. This component of the model eliminates the need to assume the ice sheet is isothermal. Varying the temperature effects the rate at which ice deforms via the Glen's Flow law. It also has the effect of increasing the temperature at the base of the glacier, producing water that can, in turn, affects the sliding of the ice due to reduced friction (basal lubrication/uplifting)

or by sediment deformation by water weakening the till. In areas of the ice sheet that are cold-based, the GSM prevents any basal sliding and till deformation from occurring as the ice becomes frozen to the bed.

3.2 Mass Balance

To calculate the ablation of the surface ice, the model uses the positive degree day (PDD) method (Tarasov and Peltier, 1999), that assumes a normal distribution of temperatures, T , centred around a monthly mean temperature, T_m , with a standard deviation σ_{PDD} . The PDD coefficients can be calculated from

$$PDD = \frac{1}{\sigma_{PDD}\sqrt{2\pi}} \int_0^{1\text{yr}} \int_0^{T_m+2.5\sigma_{PDD}} T \exp\left[-\frac{(T-T_m)^2}{2\sigma_{PDD}^2}\right] dT dt \quad (3.1)$$

The amount of ablation is proportional to the temperature-dependent PDD coefficients (Tarasov and Peltier, 2002), and any snow that remains at the end of the year is immediately converted into ice, skipping the firn stage of snow to ice transition.

The amount of accumulation depends on how much of the precipitation falls as snow, which will eventually add to the amount of ice, compared to rain which may or may not freeze somewhere down glacier from where it fell.

$$\frac{\text{accumulation}}{\text{precipitation}} = \frac{\rho_i}{\rho_w\sigma\sqrt{2\pi}} \int_0^{1\text{yr}} \int_{T_m-2.5\sigma_{RS}}^{RS} \exp\left[-\frac{(T-T_m)^2}{2\sigma_{RS}^2}\right] dT dt \quad (3.2)$$

where RS is the surface temperature of the ice, and $\sigma_{RS} = \sigma_{PDD} - 1^\circ\text{C}$ is the standard deviation

3.3 Ice Dynamics

In this model, ice deforms under stress via Glen's flow law formula Glen (1955)

$$\dot{\epsilon} = A(T)\bar{\tau}^n \quad (3.3)$$

Which relates the strain rate, $\dot{\epsilon}$, to the shear stress, $\bar{\tau}$. Eqn. 3.3 uses Glen's flow law exponent, $n = 3$, and the temperature-dependent Arrhenius factor (Payne et al., 2000) is taken as

$$A(T) = a \exp\left(\frac{-E_a}{RT}\right) \quad (3.4)$$

where a is a constant of proportionality, E_a is the activation energy for ice creep, R is the universal gas law coefficient, and T is the temperature. Following the work done in Huybrechts (1992), the ice velocity is given by

$$\vec{u} = \vec{u}_b - 2(\rho_s g)^n \{ \vec{\nabla}_h(z_s) \cdot \vec{\nabla}_h(z_s) \}^{(n-1)/2} \vec{\nabla}_h(z_s) \cdot E \int_{z_b}^{z_s} A(T^*(z'))(z_s - z')^n dz' \quad (3.5)$$

with E as an enhancement factor required for Glen's flow law to account for inaccuracies due to it's formulation from a small data set or failed assumptions about glacial ice such that it is isotropic and similar grain sizes, which may not be the case.

The ice thickness, H , in a given cell is governed by the shallow ice approximation (SIA) equation

$$\frac{\partial H}{\partial t} = -\vec{\nabla}_h \cdot \int_{z_b}^{z_s} \vec{u} dz + M_s(T) \quad (3.6)$$

in which the ice flux due to creep and basal sliding is vertically integrated over the depth of the ice sheet, and M_s represents the net mass balance of the ice at the surface and basal boundaries (e.g., melting and freezing).

3.4 Ice Thermodynamics

The thermodynamics of the ice sheet are governed by the time-dependent heat conduction-advection equation

$$\rho_i c_i(T) \frac{\partial T}{\partial t} = \frac{\partial}{\partial z} \left\{ K_T(T) \frac{\partial T}{\partial z} \right\} - \rho_i c_i(T) \vec{u} \cdot \vec{\nabla} T + E_d \quad (3.7)$$

with c_i representing the specific heat of ice, and E_d is the heat created from the deformation of ice (i.e., ice friction).

Basal boundary conditions will be set by frictional heating due to sliding, from geothermal heat sources, and lastly whether or not there is basal water present. The presence of basal water can remove or add heat to the system depending if water melts the ice (takes heat from ice) or refreezes to the ice (gives heat to ice). If the thermal boundary condition gives a temperature below the pressure melting point (PMP), and there is water present, then the water freezes to the ice and the temperature is increased until it reaches PMP or all the water is frozen (Johnson and Fastook, 2002). The temperature in eqn. 3.7 is not allowed to go above the PMP, any excess heat energy is converted to latent heat which melts the ice. Once the corrected basal temperature is found, the temperature profile is recalculated with the corrected basal temperature as the new basal boundary condition.

Chapter 4

Formulation of the Basal Hydrology Model

4.1 Discretization of the Mass Balance Equation

4.1.1 The Governing Equation

The model uses the mass continuity equation for subglacial water. Written in conservative form, the equation is

$$\frac{\partial w}{\partial t} + \vec{\nabla} \cdot \vec{Q} = \dot{b}_s + b_{2b} + d_{sa} \quad (4.1)$$

with w being the water thickness, \vec{Q} being the water flux, and the rest being source terms derived from surface and englacial meltwater entering the base, melting at the base from the basal energy balance, and exchange with the aquifer respectively.

4.1.2 Expanding the Terms

Expanding the divergence of the flux terms

$$\frac{\partial w}{\partial t} = \frac{1}{r \cos \theta} \left[\frac{\partial(Q_\phi)}{\partial \phi} + \frac{\partial(Q_\theta \cos \theta)}{\partial \theta} \right] + \dot{b}_s + b_{zb} + d_{sa} \quad (4.2)$$

with θ representing the latitudinal direction, and ϕ representing the longitudinal direction.

Next eqn. 4.2 is integrated over the finite-control volume

$$\iint \frac{\partial w}{\partial t} dV = \iint \left\{ \frac{1}{r \cos \theta} \left[\frac{\partial(Q_\phi)}{\partial \phi} + \frac{\partial(Q_\theta \cos \theta)}{\partial \theta} \right] + \dot{b}_s + b_{zb} + d_{sa} \right\} dV \quad (4.3)$$

using $dV = r^2 \cos \theta d\phi d\theta$, eqn. 4.3 becomes

$$\begin{aligned} \iint \frac{\partial w}{\partial t} dV &= \int_n^s \left\{ \int_e^w \frac{\partial(Q_\phi)}{\partial \phi} d\phi \right\} r d\theta + \int_e^w \left\{ \int_n^s \frac{\partial(Q_\theta \cos \theta)}{\partial \theta} d\theta \right\} r d\phi \\ &+ \iint \left\{ \dot{b}_s + b_{zb} + d_{sa} \right\} dV \end{aligned} \quad (4.4)$$

Using the fundamental theorem of calculus $\int_a^b \frac{\partial F}{\partial x} dx = F(b) - F(a)$ gives

$$\begin{aligned} \iint \frac{\partial w_P}{\partial t} dV_P &= \int_n^s \{Q_w - Q_e\} r d\theta + \int_e^w \{Q_s \cos \theta_s - Q_n \cos \theta_n\} r d\phi \\ &+ \iint \left\{ \dot{b}_s + b_{zb} + d_{sa} \right\} dV_P \end{aligned} \quad (4.5)$$

where the subscripts n, e, s, w stand for north, east, south, and west interfaces respectively, and P represents the central grid point.

Using the approximation $V_P = r^2 \cos \theta_P \Delta\phi \Delta\theta$, section B.1 in the appendix ap-

proximates eqn. 4.5 as

$$\frac{\partial w_P}{\partial t} = \frac{1}{r \cos \theta_P \Delta \phi} \{Q_w - Q_e\} + \frac{1}{r \cos \theta_P \Delta \theta} \{Q_s \cos \theta_s - Q_n \cos \theta_n\} + \dot{b}_s + b_{zb} + d_{sca} \quad (4.6)$$

4.2 Advancing the Mass Balance Equation in Time

The model presented in this paper uses two predictor-corrector schemes, namely Heun's method and the leapfrog-trapezoidal scheme, to advance the model through time, and uses the explicit values for the source terms throughout the discretization. The two schemes are considered predictor-corrector schemes, because each scheme will first predict the solution for the next time step and then will use that result in combination with the old values to give a better prediction of the solution at the next time step (the corrected solution).

The first scheme is Heun's method. The first step in Heun's method is to take some initial conditions (w_P^0), and to do an Euler Forward scheme for the first time step,

$$w_P^{1*} = w_P^0 + \frac{\Delta t}{r \cos \theta_P \Delta \phi} \{Q_w^0 - Q_e^0\} + \frac{\Delta t}{r \cos \theta_P \Delta \theta} \{Q_s^0 \cos \theta_s - Q_n^0 \cos \theta_n\} + (\dot{b}_s + b_{zb}^0 + d_{sca}^0) \Delta t \quad (4.7)$$

where w_P^{1*} is the tentative (predicted) values for the first time step. With the predicted values for the first time step (w_P^{1*}), the model can be iterated with a trapezoidal scheme

between w_P^0 and w_P^{1*} to convergence to give the final (corrected) value

$$w_P^1 = w_P^0 + \frac{\Delta t}{2r \cos \theta_P} \left\{ \frac{Q_w^0 - Q_e^0}{\Delta \phi} + \frac{Q_s^0 \cos \theta_s - Q_n^0 \cos \theta_n}{\Delta \theta} \right\} \quad (4.8)$$

$$+ \frac{\Delta t}{2r \cos \theta_P} \left\{ \frac{Q_w^{1*} - Q_e^{1*}}{\Delta \phi} + \frac{Q_s^{1*} \cos \theta_s - Q_n^{1*} \cos \theta_n}{\Delta \theta} \right\} + (b_s^0 + b_{sb}^0 + d_{sca}^0) \frac{\Delta t}{2}$$

The advantage Heun's method has over a regular Euler forward method is that the trapezoidal scheme increases its accuracy quadratically with decreased time steps, whereas the Euler method increases accuracy linearly. Alone, the Euler method would either overestimate or underestimate the fluxes depending on the concavity of the solution as it advances in time. Heun's method calculates the fluxes at both the present (as Euler does) and from the future (the predicted guess), then calculates the average of the two, readjusts the predicted values using the new slope, and repeats until convergence (Mathews and Fink, 2004).

Now that there are values for the first two time steps, the model will then proceed to use the leapfrog-trapezoidal scheme in favour of Heun's method. This scheme is considered to be stable and robust, even reducing the troubles the leapfrog scheme can have with diffusion equations and decoupling (Shchepetkin and McWilliams, 2005). In this scheme, the leapfrog time-stepping scheme is used to calculate predicted values for the next full time step, $w^{(m+1)*}$,

$$w_P^{(m+1)*} = w_P^{m-1} + \frac{2\Delta t}{r \cos \theta_P} \left\{ \frac{Q_w^m - Q_e^m}{\Delta \phi} + \frac{Q_s^m \cos \theta_s - Q_n^m \cos \theta_n}{\Delta \theta} \right\} \quad (4.9)$$

$$+ 2(b_s^0 + b_{sb}^0 + d_{sca}^0)\Delta t$$

where $m = 2, 3, 4, \dots$. From the predicted values, the trapezoidal scheme is applied

Variables	
Name	Represents
A_f	Areal fraction of saturated sediment
b_s	Englacial water source entering the base
b_{s_0}	Basal water production from basal melting
d_{sca}	Basal water drainage into underlying aquifer
Δt	Time step
dV	Volume element of grid cell
K	Hydraulic conductivity of sediment
L	Latent heat of fusion for ice
θ	Latitudinal coordinate
ϕ	Longitudinal coordinate
P	Basal water pressure
P_I	Ice overburden pressure
Q	Horizontal basal water flux
r	Radius of the Earth
u_b	Basal sliding velocity
w	Basal water thickness
z_0	Bed rock topography
Z_h	Bedrock bump height

Table 4.1: List of the variables used in the model description.

once again to give the corrected values, w^{m+1} , as

$$\begin{aligned}
 w_p^{m+1} = & w_p^m + \frac{\Delta t}{2r \cos \theta_p} \left\{ \frac{Q_w^m - Q_c^m}{\Delta \phi} + \frac{Q_s^m \cos \theta_s - Q_n^m \cos \theta_n}{\Delta \theta} \right\} \\
 & + \frac{\Delta t}{2r \cos \theta_p} \left\{ \frac{Q_w^{(m+1)*} - Q_c^{(m+1)*}}{\Delta \phi} + \frac{Q_s^{(m+1)*} \cos \theta_s - Q_n^{(m+1)*} \cos \theta_n}{\Delta \theta} \right\} \\
 & + (b_s^0 + b_{s_0}^0 + d_{sca}^0) \Delta t
 \end{aligned} \tag{4.10}$$

For the subsequent time steps the model will repeat the leapfrog-trapezoidal until the final time step has been reached.

4.3 Darcian Water Flux, \vec{Q}

The model uses a Darcian flux equation to represent the flow of water in a distributed drainage system. The model assumes, for testing purposes, that there is an underlying layer of till sediments that allows the water to flow along the base of the ice (see section 4.6 for discussion on this simplification). This layer of sediments is different from an underlying aquifer, that would be separated from the till by an aquitard layer (Flowers, 2000).

The flux term, \vec{Q} , is given by

$$\vec{Q} = -\frac{K_w}{\rho_w g} \vec{\nabla} \{P + \rho_w g z_b\} \quad (4.11)$$

where K is the hydraulic conductivity of the underlying till, z_b is the topographical bed elevation, and P is the water pressure beneath the ice.

Looking at the flux on the westward edge of a grid cell, Q_w , we get

$$Q_w = \frac{K_w P_W - P_P + \rho_w g (z_{b_w} - z_{b_P})}{\rho_w g r \cos(\theta_P) \Delta\phi} \quad (4.12)$$

where the W subscript indicates the value of the grid point to the west of the central point, and the P subscript represents the centre grid cell.

Since the flux is defined at the interface between two grid cells, the value for w in eqn. 4.12 will be determined using the upwind scheme (Patankar, 1980), which assigns w the value from the grid cell with the greatest hydraulic pressure. Following Patankar (1980), K is set to the harmonic mean of the hydraulic conductivity at the

two grid points, which gives (see appendix B.2)

$$Q_w = \left(\frac{2K_W K_P}{K_W + K_P} \right) \left(\frac{1}{\rho_w g r \cos(\theta_P) \Delta\phi} \right) \left[\begin{aligned} & \max\{w_W[P_W - P_P + \rho_w g(z_{b_W} - z_{b_P})], 0\} \\ & - \max\{-w_P[P_W - P_P + \rho_w g(z_{b_W} - z_{b_P})], 0\} \end{aligned} \right] \quad (4.13)$$

Q_w is positively defined if water flows eastward into the centre grid cell. Similar equations for fluxes through the other three grid cell faces are given in appendix B.2.

4.4 Hydraulic Conductivity

Being a dilatant material, the hydraulic conductivity of till varies according to the water pressure in the pore space. As water fills the pores, the increased water pressure expands the pore space, which causes the hydraulic conductivity of the till to increase.

The hydraulic conductivity for this model is taken from Flowers (2000). In her analysis she tries to parameterize the subgrid properties of the till that affect hydraulic conductivity, such as the interconnectivity of the pores. The two topographical factors on hydraulic conductivity are the amplitude of the bumps in the bed and their wavelength. Flowers relates these to properties to power and correlation in the spectral domain. A decrease in power (amplitude of the bumps) or an increase in correlation will lead to an increase in the hydraulic conductivity, and vice versa.

From her spectral analysis, and using the “upstream donor cell” method (Zevenbergen and Thorne, 1987) to act as a proxy, Flowers attempts to determine how connected the pores in a grid cell are. The analysis shows that the pore space, and hydraulic conductivity, depends on the type of material in the till (e.g., sand or clay), and the water pressure that acts to open up pores as the pressure builds. The analysis

also shows that the hydraulic conductivity will exhibit a transitory nature where at low water pressures the conductivity will be low and then at some critical value the conductivity will start to dramatically increase to the maximum conductivity the material will allow. Flowers parameterizes the hydraulic conductivity, K_p , as a function of water layer thickness (as a proxy for pressure) as

$$\log(K_p) = \frac{1}{\pi}(\log[K_{max}] - \log[K_{min}]) \tan^{-1} \left[k_a \left(\frac{w_p}{h_c} - k_b \right) \right] + \frac{1}{2}(\log[K_{max}] + \log[K_{min}]) \quad (4.14)$$

where the hydraulic conductivity can vary between a maximum value, K_{max} , and a minimum value, K_{min} , that vary depending on the study site and its till composition (e.g., higher values for sandier till and lower values of clayier tills). The \tan^{-1} function acts to mimic the transitory nature of the hydraulic conductivity from Flowers's analysis. The effects of k_a and k_b are illustrated in fig. 4.1. The parameter k_a changes the sharpness of the transition, as k_a is increased the transition from low conductivity to high conductivity becomes more sharply defined. The parameter k_b is used to adjust when the transition from low to high conductivity occurs, in terms of the ratio of w_p/h_c .

4.5 Water Pressure

Flowers (2000) uses data from 552 boreholes drilled on Trapridge Glacier over a 12 year span from 1985-1997 to derive a statistically-based water pressure formulation. The statistical analysis of the bore hole data is much too complex to go into detail here; further reading can be found in chapter 4 of Flowers (2000). Presented here is a quick summary of the main ideas from the analysis.

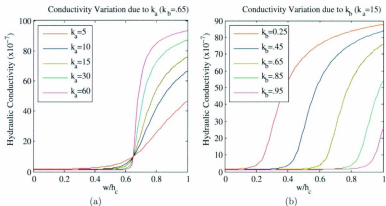


Figure 4.1: Variations of subglacial hydraulic conductivity K with respect to changes in hydraulic parameters k_a and k_b for values of K ranging between 1.0×10^{-7} – 1.0×10^{-5} .

From the data, the spatial trend of the bed topography, z_b , is removed via best-fit lines in the northward and eastward directions, leaving the anomalies, δz_b . The anomalies are considered to be independent of position (i.e., the same in all grid elements), and are completely filled in with sediment, as shown in figure 4.2.

Flowers (2000) assumes, for simplicity, that cavities that would form underneath the ice are filled in with sediments. As she states, sediment patches and cavities are likely to coexist, but there would be a tendency for cavities to be filled by sediments. This assumption allows the areal fraction of saturated sediment to be directly taken from the cumulative distribution function and scaled by the grid average porosity. The maximum amount of water that can be in a cell depends on the anomaly (sediment) thickness and porosity, which gives the areal saturation.

From her analysis, Flowers derives an expression for the areal fraction of saturated sediment, A_f , as a function of basal water thickness, based on a modified Maxwell distribution of the bed anomalies (Flowers (2000) eqn. 4.6). Flowers proposes that

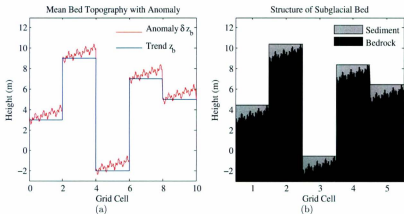


Figure 4.2: a) shows the bed topography separated into a trend and anomaly. b) The gaps in the anomalies are filled in with sediment where the hard bedrock and soft sediment make up the underlying substrate.

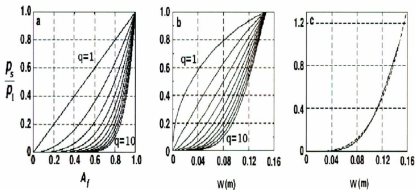


Figure 4.3: Proposed relationships for a) P with respect to A_f , b) P with respect to w , and c) analytic approximation (eqn. 4.15) to curve of $q = 10$. Image modified from Flowers (2000) with permission.

the relation between the water pressure and areal fraction of saturated sediment be of the form $P_p = P_{I_p} A_f^q$, where P_I is the ice overburden pressure; the relationship is shown in fig. 4.3a for different values of q . An expression of $P(w)$ is also derived (modified from Flowers (2000) eqn. 4.5) and the function is shown in fig. 4.3b.

It is likely that if there is a small amount of water present in the sediment then the water pressure will be low, but it should quickly rise as the sediment pore space becomes filled. This is because as the pore space fills up, there will be greater pressure build up as water compresses to allow more water to enter the pores. Assuming that water is incompressible, then the water pressure, P , will increase rapidly as the pore space fills up. For this reason it is likely that the value of q should be high ($q \geq 5$); Flower's chooses the value of $q = 10$, since fig. 4.3b shows this behaviour at high values of q . Flowers then approximates the $q = 10$ curve by the equation

$$P_p = P_{I_p} \left(\frac{w}{h_c} \right)^{7/2} \quad (4.15)$$

where h_c equals till thickness times porosity, and is effectively the water thickness that the till can hold before becoming over-saturated. For example, a till layer 5 meters thick with a porosity of 0.4 could hold a layer of water 2 meters thick ($h_c = 2m$). From fig. 4.3c, this equation has the properties of having low pressures for small water thickness and blows up rapidly as the sediment water capacity beings to fill up.

4.6 The saturated sediment parameter, h_c

During the testing of the model in this project, the sediment thickness is set to a constant value over the entire bed of the NAIC. While this should be acceptable for model testing purposes, it is not a realistic assumption about sediment cover underneath an ice sheet. This could cause problems if the sediment parameter is recast

as a variable that is allowed to have zero thickness in places (no till present). One simple prescription is to set it to a infinitesimal value (to avoid numerical infinities) and simply allow the water to be at ice overburden and channelized systems to always form over hard rock, such as the Canadian Shield. This is certainly a viable option, but the concept behind this model is that the Darcian flow represents all forms of distributed system, such as linked-cavities that can exist on hard rock (Kamb et al., 1985; Fowler, 1987; Fountain and Walder, 1998; Flowers, 2000; Johnson, 2002). Since linked-cavities are formed on the leeward side of bumps in the bedrock (Z_b), then an one potential solution is to set the minimum value of h_c to the bump height. This will allow the cavities to retain their water in the absence of till, allowing basal water pressures to be calculated, and water movement in a distributed drainage system.

4.7 Tunnel Flow

The formation of tunnels underneath the ice depends on the water flux between the cavities. As the flux increases, the friction of the water on the ice causes it to melt and if this melting continues then a tunnel can form.

4.7.1 Theory

The model developed by Schoof (2010) considers a drainage system consisting of linked-cavities and R-channels, in the same way that Kamb (1987) and Walder (1986) studied the drainage system. The equations Schoof uses are similar to Kamb's, except for Schoof uses a non-linear rheology ($n = 3$ in Glen's flow law) and Kamb uses a Newtonian rheology ($n = 1$). For cavity formation it is assumed that heat dissipation is negligible and that cavity opening and closing only depends on water pressure opening the cavity and ice deformation trying to close it. In the steady state this can

be written as

$$S = \frac{|\bar{u}_b|Z_h}{K_v p_{eff}^n} \quad (4.16)$$

where u_b is the basal sliding velocity, Z_h is the size of the bumps in the bedrock. This is eqn. 2.5 solved with $\partial S/\partial t = 0$ and ignoring the melting of the wall (first term on the right hand side). Which has the cavity-like property of increasing S with decreasing p_{eff} .

To test the stability of the model, eqn. 2.5 is written as

$$v_m(S, \Phi) = |\bar{u}_b|Z_h + \frac{C}{\rho_w L} S^\alpha |\bar{\nabla}\Phi|^{3/2} \quad (4.17)$$

$$v_c(S, \Phi) = K_v p_{eff}^n S \quad (4.18)$$

$$\frac{\partial S}{\partial t} = v_m(S, \Phi) - v_c(S, \Phi) \quad (4.19)$$

with v_m refers to the opening velocity of the cavity/tunnel, v_c refers to the closure velocity of the cavity/tunnel, L as the latent heat of fusion for ice, and $\alpha = 5/4$. \bar{Q} from eqn. 2.5 was replaced with the Darcy-Weisbach equation for turbulent flow in a circular pipe (a different version of Darcy's law than was used in Flowers (2000)). The constant $C = 2^{1/4} \sqrt{\pi + 2} / (\pi^{1/4} \rho_w f)$ is related to the shape of the tunnel and the Darcy friction factor, f .

By perturbing the cross-sectional area in eqn. 4.19, the analysis shows that the cavity is unstable if

$$\frac{\partial v_m}{\partial S} - \frac{\partial v_c}{\partial S} > 0 \quad (4.20)$$

It is then reasoned that this instability is the same as

$$\frac{\partial \bar{p}_{eff}}{\partial \bar{Q}} > 0 \quad (4.21)$$

that is the effective pressure increases (water pressure decreases) as the mean flux, \bar{Q} , increases. As mentioned in sec. 2.2.2 this is how R-channels behave, which causes them to form arborescent, channelized systems. Further analysis (see Schoof (2010) supplementary material) shows the effective pressure can be defined as

$$\bar{P}_{eff}^n = \frac{(\rho_w L) \bar{Q} \bar{\nabla} \Phi + u_b h}{K_v C \bar{Q}^{1/\alpha} \bar{\nabla} \Phi^{-1/(2\alpha)}} \quad (4.22)$$

and by taking the derivative with respect to \bar{Q} the condition for tunnel flow is given as

$$|\bar{Q}| < \frac{|\bar{u}_b| Z_h}{(\rho_w L)^{-1} (\alpha - 1) \bar{\nabla} (P + \rho_w g z)} \quad (4.23)$$

which says that if the flux through the cavity, $|\bar{Q}|$, is less than the equation on the right hand side then the cavity is stable. Otherwise, when $|\bar{Q}|$ exceeds this condition, the cavity is unstable and a tunnel will form.

4.7.2 Implementation

To simulate the change between different drainage systems, at regular user-defined intervals, the hydrology model checks the water fluxes to see if they are greater than the critical flux from eqn. 4.23, at which point it will mark the source cell as a tunnel cell. From here the model employs a down hydraulic gradient solver (Tarasov and Peltier, 2006) that looks at the neighbours of a tunnel cell and allows water to flow down the path of steepest potential gradient until there is no cell with a lower hydraulic potential or the water exits the ice sheet.

Any cell that cannot drain its water because its neighbours are all at a higher potential becomes a lake and will build up water until its potential exceeds one of

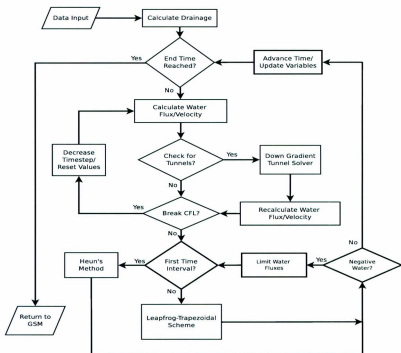


Figure 4.4: Hydrology model flow chart highlighting the processes involved in simulating basal water flow.

its neighbours and then one of the neighbours will become a tunnel cell. The solver will ultimately map out a system of tunnels beneath the ice where the tunnels will either lead into a subglacial lake or exit the terminus of the ice sheet. The tunnel solver treats the water with hydrostatic pressure where a 1 metre water level drop corresponds to a 1 metre drop in hydraulic head. The solver moves the water in the tunnel system, adjusting the hydraulic head, until all the water leaves the ice sheet or is trapped in a lake (Tarasov and Peltier, 2006).

4.8 The Source Terms

From eqn. 4.1, the first source term, \dot{b}_s , is the influx of water from any water that reaches the base from the englacial flow of water (e.g., water entering the base via crevasses or moulins). Due to this being the first implementation of physically-based subglacial hydrology into the GSM (along with size of the grid cells for current continental scale contexts), there is currently no surface input of water into subglacial hydrology model. In the current GSM, the surface melt water flows along the surface until it forms supraglacial lakes or runs off the edge of the ice sheet.

The second source term, b_{zb} , is the basal water source due to melting at the base of the ice sheet. The sources of energy at the base of the ice sheet come from ice thermodynamics, basal sliding creating frictional heat, deformational heating of the ice as it undergoes creep, and geothermal heat from the bed, as discussed in chapter 3.

The last term, d_{sa} , refers to the drainage of water from the ice-bed interface down into an underlying aquifer. In this project, the drainage is defined using a drainage parameter, D_r , that removes a percentage of the water in a cell (Johnson, 2002). At the beginning of each call to the hydrology model, the value for d_{sa} in each cell is defined as a percentage of the current water (before any new calculations are done), and is kept constant throughout the entire hydrology simulation and is updated upon the next call to the model. Note, that distributed (Darcy) flow system partly represents flow through an underlying sediment layer which is distinct from the aquifer component.

This assumption assumes all water in the aquifer is drained and that water cannot re-emerge from the aquifer back into the ice-bed interface. The work of Lemieux et al. (2008) suggests that the average rate of water infiltration into the aquifer is around 2.5 mm/yr, ranging from 0–6 mm/yr. In the GSM simulations in chapter 6, the majority

of water thickness is near 0.33 m. With the baseline value of 2.00% drainage would suggest a drainage of 6.60 mm/yr, which is slightly above the maximum values from Lemieux et al. (2008). However, for areas with thicker water levels (e.g., The Hudson Bay Ice Stream), the aquifer drainage would be well in excess of the maximum values. A second problem with the simplified aquifer is that it assumes similar drainage everywhere. The infiltration rates of the aquifer vary, in part, due to the type of substrate the ice is lying on. The aquifer drainage on the Canadian Shield will be much less than drainage in the prairies. This is due to the poorer infiltration rates of the Shield rock compared to the prairie sediment layer (Lemieux et al., 2008). Lastly, this simple parameterization of the aquifer does not allow the aquifer to return water to the basal system (known as recharging or exfiltration). Lemieux et al. (2008) calculated that the exfiltration rates to be 12 mm/yr. This water would enter into areas of the base that would pressurize that area and affect ice dynamics, or into a channelized system where it could drain out of the ice sheet. One small justification for the drainage parameter is due to the large scales involved. Over a resolution of 40 km grid cells, it is not expected that the water will be evenly distributed over the grid. The subgrid distribution of water would be stored in packets of water (e.g., in cavities or lakes) which would be under higher pressures, promoting aquifer drainage.

Despite the problems with the simplified aquifer, this simple assumption removes several complexities from the model, simplifying the study of the basal drainage system (e.g., understanding the role of linked-cavity and tunnel in water movement).

4.9 Flux limiting

Due to the numerics of the solution, there is a possibility that in a given time step there may be more water draining from a cell than there is in the cell. While negative

water levels may be an acceptable numeric answer to the discretized equations above, they are not physically acceptable answers. To alleviate this problem the fluxes of water leaving the cell are limited so that the water level in the cell remains at zero or slightly above (from rounding).

To do this the model determines how thick the negative water level in the cell is. Then, looking only at the fluxes that remove water, determines how much each lowers the water level. From this information, each flux is multiplied by a fraction between 0 and 1 to limit its flux. For example, consider a 1-D case with no aquifer drainage. Let a cell have a 3 m thick layer of water in the beginning. The flux to the left removes 2 m and the flux to the right removes 3 m, leaving the cell with -2 m. The total outgoing flux is 5 m, so the multiplier to the fluxes becomes $|-2|/5 = 0.4$. So the flux on the left removes $0.4(2\text{ m}) = 0.8\text{ m}$ and the flux on the right removes $0.4(3\text{ m}) = 1.2\text{ m}$, leaving the cell with no water.

Chapter 5

Model Validation

5.1 Introduction

When developing a new model, it is essential that the model be tested and evaluated to confirm that the model works properly. When possible, it is best to run and compare the model to either a real-world example (e.g., against data collected from the field) or to an equation that has an analytic solution. Like any scientific theory, these validations do not allow one to say that the model is correct, but it does give a basis from which the model can be used with confidence as a tool to aid in the study of glaciology, and climatic changes in general.

The problem with validation of the proposed model is that there is sparse data on subglacial hydrology due to the difficulties of obtaining the data, such as not being able to directly observe water flow under ice; cold and harsh environments (e.g., Antarctica and Greenland ice sheets); and ice sheets no longer existing (e.g., Laurentide and Scandinavian ice sheets). Also, the equations of water flow, even for the most simple cases, are highly non-linear partial differential equations that cannot be solved analytically.

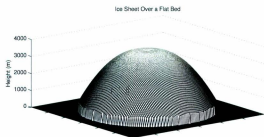


Figure 5.1: Final dimension of the ice dome used in model testing (for a flat topography).

However, as a proxy to true validation, the model can be evaluated using simple ice sheet profiles and bed topographies to judge if the model behaves as expected under those conditions.

The continental-scale ice sheet model used in most of these tests has a parabolic profile from the centre of the ice sheet to the terminus and is symmetric around the centre (i.e., bowl-shaped ice sheet), according to the equation

$$\begin{aligned}
 H(d) = & (-4H_{mid} + 2H_{max} + 2H_{min}) \left(\frac{d}{r_t} \right)^2 \\
 & + (4H_{mid} - 3H_{max} - H_{min}) \left(\frac{d}{r_t} \right) + H_{max} \quad (d < r_t)
 \end{aligned} \tag{5.1}$$

where H_{max} is the ice thickness at the ice divide (the centre), H_{min} is the thickness at the terminus, H_{mid} is the thickness at half-way down the glacier (used to define how sharply the glacier decreases from H_{max} to H_{min}), d is the distance from the ice divide, and r_t is the distance to the terminus. In the model runs, the ice sheets starts from the ground (at $t_{now} = 0$) and grows until 50% of the model runtime (t_{half}). The ice thickness grows according to eqn. 5.1 multiplied by the ratio t_{now}/t_{half} . When t_{now}

is greater than t_{half} , the ice sheet is at it's maximum size (as shown in fig. 5.1).

To facilitate the growth of the subglacial hydraulic system, a constant melting at the base of the ice is applied in a 'ring' of uniform thickness near the terminus, with 0.6 m/yr of melting at the terminus and decreasing linearly to 0.4 m/yr at the inside of the 'ring'. However, if there is no ice where the ring of melt water is defined, then the value of melt, M_d , is set to zero until there is ice, in which case it would take the value defined from the equation

$$M_d(d) = M_t - (M_t - M_i) \left(\frac{r_t - d}{c_r} \right) \quad (r_t - c_r < d < r_t) \quad (5.2)$$

where M_t is the melt rate at the terminus, M_i is the melt rate on the inside of the melt ring, and c_r is the thickness of the ring from the terminus into the inner most melting point.

To evaluate the model, the ice sheet will be placed on different bed topographies to study the effects of how it affects water flow and storage. The bed topographies to be tested are a flat bed, an inclined plane, an inclined plane in a v-shaped valley, and a dilating bed. These test are designed to test for the symmetry of water flow (when it should exist), that water does not flow into the core of the ice sheet, flows down the potential gradient, and can form lakes.

5.2 Mass Conversation and Symmetry of Darcian Flow

For the first set of tests, the tunnel formation code is turned off to test the Darcy flow for conservation and symmetry as the tunnel code is known to potentially cause slight asymmetry (Tarasov and Peltier, 2006).

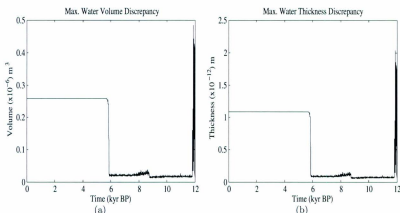


Figure 5.2: Water Gain/Loss represented as a) maximum volume loss in cell and b) maximum water thickness discrepancy in a cell.

5.2.1 Study 1: Ice Sheet on a Flat Bed

The first model test is for mass conservation. The set-up for this test has the ice sheet on a flat bed topography, the same as fig. 5.1, and the water imbalance of each cell is recorded. The test results for mass conservation are shown in fig. 5.2. Fig. 5.2a shows that the numerical water loss in a cell reaches values of the order of 10^{-7} m³. Putting this in terms of water thickness discrepancy, fig.5.2b shows that the maximum difference between the mass balanced answer and the modelled answer differ only by 10^{-12} m. This confirms mass conservation of the Darcy component.

The next requirement is that the model conserves symmetries. Due to the flat topography and perfectly round, parabolic ice sheet, the model should have complete radial symmetry about the centre of the ice sheet. From fig.5.3a, the water distribution beneath the ice sheet shows signs of symmetry around the ice sheet. What may look like a slight asymmetry between north and south is due to the model being run in spherical coordinates, causing the figure to flatten as it approaches the pole.

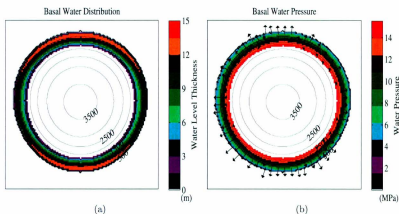


Figure 5.3: a) Basal water distribution after 20kyr run with an ice sheet resting on a flat bed, and b) the basal water pressure with arrows indicating the direction of water movement. Water moves radially away from the centre of the ice sheet perpendicular to areas of constant basal pressure according to eqn. 4.15.

Fig 5.3b shows the basal water pressure is higher in the interior of the ice sheet where the ice is thicker. This higher pressure causes the water to flow radially outward from the interior, as indicated by the flowlines. These results are expected since the thicker ice drives the water to flow toward the terminus of the ice sheet, leading to thicker levels of water near the edges. The model results also show that the water levels are rather thick, indicating a lot of water storage. This can be attributed to the exclusion of tunnel formation leaving only the inefficient, distributed drainage system to remove the water.

5.2.2 Study 2: Ice Sheet on an Inclined Plane

Now that mass conservation holds and radial symmetry exists for the flat topography, the next test is designed to see how water behaves in a potential gradient. In this test, the ice sheet is placed on an inclined plane with a degree of inclination $\approx 0.05^\circ$,

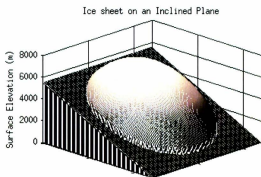


Figure 5.4: Final set-up to test the downward flow of water.

as shown in fig. 5.4. As was the case in the mass balance test, the ice melts at the base in a 'ring' near the terminus.

Due to the inclusion of an incline, the basal water distribution in fig. 5.5a does not have the same radial symmetry as the flat bed case. In this scenario, the incline prevents symmetry between the northern and southern halves of the ice sheet. This occurs because the water on the northern side has to run uphill to escape from the ice sheet, whereas the water on the southern side has an easier path downhill to exit the ice sheet. This results in the water to the north being a little bit thicker than the water on the southern side. The distribution of water thickness stills shows the symmetry between the east and west halves. This is expected since the hill runs perfectly north to south which should not have an effect on the east/west flow of water.

This study examined how water movement is affected by changing the bed slope. Water exits the ice sheet due to the potential field created by the ice sheet. On the north side of the ice sheet, the slope of the bed created a potential field to counter the outward flow of water. However, the hydraulic potential pressure of the basal water

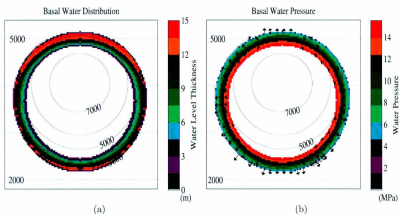


Figure 5.5: a) Basal water distribution after 20kyr run with an ice sheet resting on an inclined plane, and b) the basal water pressure and flow lines showing faster flowing water on the south side of the ice sheet.

in fig. 5.5b is able to overcome the retardant back pressure of the bed and still flow out. On the other hand, the potential field on the south side of the ice sheet acted to increase the basal water velocity, resulting in there being less water in the south.

5.2.3 Study 3: Ice Sheet in a Valley

To further investigate water's ability to flow, the ice sheet is kept on an incline plane, as before, but this time there are valley walls that cuts through the ice sheet along the east and west sides. This test is designed to expand on the last test to see what happens when the water on the north side of the glacier cannot get to flow to the south side and escape (due to water having to flow into the interior of the ice sheet to flow south). The model is ran with the same conditions from the last study with the inclusion of a barrier blocking water flow out the sides of the ice sheet, to see how the water distribution changes. The steady state results of this study are shown in

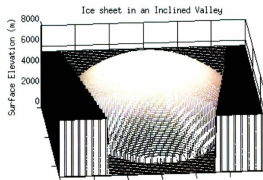


Figure 5.6: Final set-up to test the flow of water down a potential gradient.

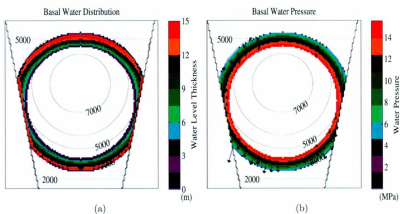


Figure 5.7: a) Water distribution of an ice sheet in a valley that restricts the flow of water from flowing out the sides of the ice sheet. b) The corresponding basal water pressure.

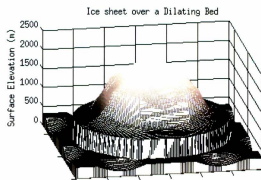


Figure 5.8: The final setup to test the formation of lakes in potential wells underneath the ice sheet.

fig. 5.7, and the results show that there is little difference between this study and the previous study without the valley walls.

The basal water distribution in this setup is similar to the previous setup. In fig. 5.7a the water that would have left on the sides of the ice sheet now has to flow southward to exit the ice sheet. This results in a thicker water distribution along the walls of the valley and south-east and south-west sides of the ice sheet that were not present when there was no valley.

Despite the changes in water thickness, the basal water pressure remains unchanged due to it being at ice overburden pressure. In fig. 5.7b, the water flow from the east and west sides of the ice sheet down to the south are rather slow. The water has to flow close to the interior of the ice sheet, where the basal pressures are higher, which provides more resistance to water flowing.

5.2.4 Study 4: Ice Sheet Over a Dilating Bed

The previous two tests showed that the model properly allows water to flow down gradient and does not enter the cold-based section of ice. With the flow of water taken care of, this test was designed to stop the flow of water and test the model's ability to form lakes. According to Paterson (1981), the hydraulic pressure gradient, $\vec{\nabla}\Phi$, is given by

$$\vec{\nabla}\Phi = \rho_i g \vec{\nabla}z_s + (\rho_w - \rho_i)g \vec{\nabla}z_b \quad (5.3)$$

This equation basically states that the change in the surface elevation is roughly ten times more prominent in changing the hydraulic pressure gradient than changes in the bedrock elevations. To test lake formation, the model was set up with an ice sheet over a dilating bed to facilitate the growth of lakes in the dips of the underlying bed. Since the pressure field depends so much on the shape of the ice sheet, the ice sheet was flattened near the terminus to reduce its effects on the field so that the lakes could form near the depressions in the topography under the ice sheet.

The dilating bed is a function of location and is created using the equation

$$z_b(d, \theta) = \min((z_A) \cos(30\theta) \cos(30\phi), 0) \quad (5.4)$$

where z_A is the amplitude (i.e., depth of the dip), d is the distance from the ice divide as before, and the angles θ and ϕ are needed since the dilating bed is not radially symmetric. This causes the setup not to be exactly symmetric as the northern dip is slightly outside the ice sheet, whereas the southern dip is completely underneath (east-west symmetry still exists). The ice sheet for this study, as seen in fig. 5.8, is different from the others because it uses a decaying exponential curve to smooth out the ice sheet toward the terminus. The ice sheet profile is given by the original sheet

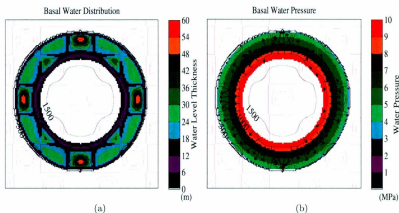


Figure 5.9: a) Water distribution showing lake formation on the south and east sides of the glaciers. b) The pressure field that acts on the basal water showing the pressure minimum located where the lakes formed and the flowlines leading water into the lakes.

from eqn. 5.1, with the modification

$$H(d) = \left(\frac{(H_s - H_d)^2}{(H_{min} + H_s - 2H_d)} \right) \exp \left[\frac{-1}{c_c} \log \left(\frac{(H_s - H_d)^2}{(H_{min} + H_s - 2H_d)^2} \right) \times \left(d + c_c - r_t \right) + \frac{(H_{min} H_s - H_d^2)}{(H_{min} + H_s - 2H_d)} \right] \quad (r_t - c_c < d < r_t) \quad (5.5)$$

with H_s is the ice thickness at the top of the curve, H_d is the ice thickness halfway down the curve, c_c is the radial length of the curve (akin to melt 'ring' thickness in section 5.1), and the other variables are as defined in section 5.1. Fig. 5.9a shows the water distribution is still symmetric about any axis drawn through the ice divide. Darcy flow, with high values of hydraulic conductivity, is able to gather the water into lakes near the edge of the ice sheet. This is because the ice surface slope has a greater impact on the hydraulic potential than the bedrock slope. Lakes form near the terminus because the shallow surface slope allows the bedrock slope to become

the dominant factor, allowing water to fill up the dips in its topography. Notably, the lakes do not form at the centre of the dips, but closer to the terminus because of the influence the surface slope still has at driving the water toward the terminus. This can be compared to the bedrock dips that are closer to the interior that form lakes at the edge of the dip or not at all, because of the steeper surface slopes that keep the hydraulic potential high enough to allow the water to continue flowing toward the terminus.

Fig. 5.9b confirms that the water pressure is much higher in the interior of the ice sheet and becomes much smoother near the terminus. The flowlines show that the water flows pass the interior dips and converge to form lakes in the dips that are closer to the edges.

5.3 Water flow beneath the ice sheet with the inclusion of tunnels

The case studies of the Darcy flow model showed that it was mass conserving and displayed symmetry (as applicable). The next set of test use the same setups as before to study the influences that a channelized drainage system can have on the subglacial environment.

5.3.1 Study 5: Ice Sheet on an Flat Bed

Enabling the tunnel solver into the flat bed scenario from section 5.2.1 greatly reduces the amount of basal water present. The most noticeable difference between this run and the no tunnel case is that symmetry becomes broken. This run is mostly symmetric, but there are a few places where the water gathered. This shows that the tunnel code is slightly non-symmetric, but this break in symmetry would most likely

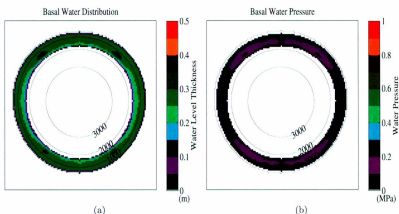


Figure 5.10: a) Tunnel formation allows much more of the water to drain from the basal environment. b) The basal water pressure is greatly reduced due to the removal of water. The addition of the tunnel code leads to symmetry being broken from section 5.2.1.

not be noticeable in real scenarios where the ice sheet and topography would not have as much symmetry as this simplified scenario.

5.3.2 Study 6: Ice Sheet on an Inclined Plane

Returning to the ice sheet on the inclined plane, fig. 5.11a shows that there is way less water present due to tunnel formation. As before, there is a clear asymmetry between the north and south of the ice sheet due to the bed slope. The water pressure in fig. 5.11b is greatly reduced from before. The reduced pressure would have important consequences on basal sliding, causing the ice to prevent shutoff of any ice surging event.

Both plots in fig. 5.11 show a checker board pattern appearing just west of the north of the ice sheet. The source of this is as follows. Currently, the tunnel solver simply drains all the water in the tunnel cells. This inhibits tunnel flow for a given

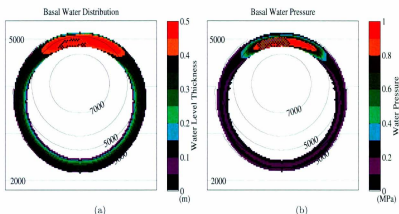


Figure 5.11: a) Tunnel formation allows much more of the water to drain from the basal environment. b) The basal water pressure is greatly reduced due to the removal of water.

grid-cell in the succeeding time step as the outward water flux from the Darcy solver will then be null (tunnel drainage condition is outward Darcy flux above a specific threshold). As such, tunnel behaviour oscillates between alternating time steps. Given the radial tunnel flow (tunnel solver permits drainage to diagonally adjacent grid cells), this results in the checker board pattern for this artificially symmetric test case.

Admittedly, complete water drainage in the tunnel solver is not a physical approach since the tunnels would close as the water pressure dropped (along with the water thickness). Also, due to the large grid size, the tunnels would not have access to all the water in the cell, meaning less water drainage. The adjustment of relevant tunnel parameters and associated sensitivity analysis will be left for future work.

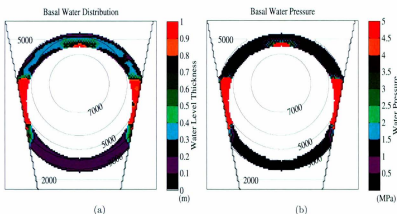


Figure 5.12: a) Tunnel formation allows the water flow much easier from the sides of the glacier to the terminus in the south. b) Basal water pressures are higher on the sides where water becomes trapped, but much lower in other parts of the ice sheet.

5.3.3 Study 7: Ice Sheet on an Inclined Plane in a Valley

As expected, fig. 5.12a shows that the tunnels greatly reduce the water levels beneath the ice. There is still some build up of water at the sides of the ice sheet as the water has to flow through higher pressures to flow southward. The formation of tunnels greatly eases this process as water build up at the sides will create low-pressure tunnels to provide excess to the terminus in the south.

The basal water pressure in fig. 5.12b is generally pretty low except at the sides and at the north part of the ice sheet. These are areas where tunnels have trouble forming due to the water becoming trapped in a hydraulic potential dip (the north is trapped due to the uphill slope and the sides are trapped by the valley forcing the water into the interior). In these cases the water has to build up in these areas until its pressure increases enough to allow the water to flow and form tunnels. This is true for the entire northern section as it battles to flow uphill (with respect to basal

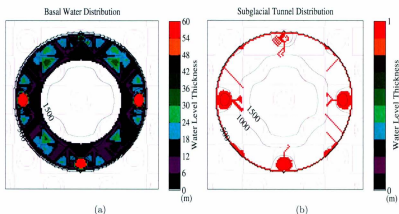


Figure 5.13: a) Basal water distribution shows the formation of larger and more numerous lakes due to the inclusion of tunnels in the Darcy model. b) The formation of tunnels converge to the lakes and all the way to the terminus at the northern dip.

topography), but it is most noticeable near true north where the slope is the steepest along a radially outward path.

5.3.4 Study 8: Ice Sheet Over a Dilating Bed

Although it cannot be determined from fig. 5.13, the lakes are much thicker than before (they are approximately 120m depth, as opposed to 60 m with only Darcy). This increase in thickness can be attributed to the increase of water flux into the lakes due to the tunnels flowing into them. The most notable feature is that the northern lake, that was in the Darcy-only test, is no longer present. With the inclusion of tunnels, the water that reached the dip was able to continue onward and out the terminus. The tunnels generally travelled toward the terminus, following the potential gradient. When two or more tunnels meet, they will converge into one tunnel and form an arborescent network.

What this study shows is that the model can create lakes under the right conditions of relatively flat ice and inverse bed slope to water flow. Another way to create a lake in the model is to surround it by cold-based ice, creating an ice-dammed lake. These results are somewhat expected as subglacial lakes are often found in areas of the ice sheet that are flat (due to the presence of water reducing the resistance of ice flow). Thus lake formation could be caused by a build up of water surrounded by cold ice (ice-dammed lake) or possibly from a distributed (e.g., linked-cavity) system formed in a topographical dip that causes ice to flow quickly over the dip and flattening the ice in the process. This could cause a positive feedback where more and more water enter the dip (e.g., from water flow into a potential well and from friction melting at the base) and form a lake.

5.3.5 Study 9: Doubling the Grid Resolution

One final test of the model is to see how well the results of the previous studies compare to the results with a finer grid. The previous studies use a grid spacing of 0.005 radians (approximately 0.30°). In this case study the ice sheet is placed over an inclined plane, as in section 5.3.2, with a grid spacing of 0.025 radians. Unfortunately, using the parameters from the previous studies lead to the model stability as the model has a user-defined minimum time step set at approximately 3 days. Since the previous studies used a parameter set with higher values for hydraulic conductivity (to emphasize the effects of potential gradients and tunnel formation). For this test the hydraulic conductivity ranges were lowered from 10^{-6} – 10^{-4} to 10^{-7} – 10^{-5} . This new parameter set did not become unstable and gave results clear enough to note the similarities and differences between the fine and coarser resolutions.

The results in 5.14 show a striking similarity to each other. They both show that water in the north is thicker than in the south, and they have the same distinguishing

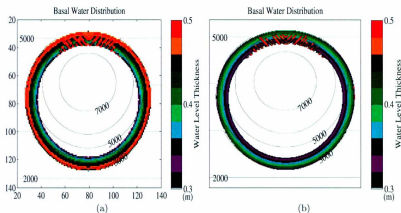


Figure 5.14: a) Model result with resolution at 0.30° . b) Model result with resolution at 0.15° .

strips of thicker water in the north. The simulation with the higher resolution shows a universal trend of thinner water with a drop of about 20% in water levels near the terminus (this drop decreases toward the interior). What this shows is the importance of grid resolution, but for continental-scale modelling this will probably only have a minor affect on the timing of certain events (e.g., tunnel formation), and little change to the general patterns of ice sheet and basal hydrology evolution.

5.4 A quick overview of the validation results

The previous validation tests were designed to explore the properties of the basal hydrology model. Using simplified ice sheets allows the emerging patterns of water flow and distributions to be compared to the expected results in these idealized scenarios.

The model was tested for mass conservation. The results in section 5.2.1 show that the model is mass conserving on the order of 10^{-12} m of water thickness within

a grid cell.

The results also show that water flows down potential gradients with the ice surface slope showing dominance over the bed slope. In areas where the ice is relatively flat and there is a dip in the bed, the hydrology model does allow for the build up of water into subglacial lakes.

The inclusion of the tunnel solver allows the water to move around more effectively beneath the ice, which results in less basal water available. Also, over the dilating bed, the lakes gathered more water from a larger area rapidly, resulting in deeper lakes with larger areal extent.

The doubling of the model resolution shows an ice sheet with slightly less water. Despite the changes in water thickness, the model shows similar behaviour, suggesting that doubling the resolution would not have much of an impact on the results.

Chapter 6

One-way Coupling of the Hydrology Model to the GSM

Having validated the model and showing some of the water behaviour for simplified ice sheets, the next step is to couple the model to the full GSM to see how the water behaves under more complex forcing conditions. The aim of this study is to determine the most important parameters so that further efforts in obtaining data can be focused on constraining the most prominent parameters, and less effort on the least prominent ones. This section highlights some of the main results of the GSM runs, in depth details of the runs can be found in appendix A.

The first step in understanding how ice sheets and basal hydrology interact is to one-way couple the two and see how ice affects water behaviour without the water affecting the ice. This will allow the results from the GSM to be compared to the simplified results from section 5. As before, a series of model runs with varying parameters will be used to study the sensitivity of the model to changing parameters.

List of Model Parameters			
	Represents	Value	Reference
F_{CFL}	Prevents breaking CFL	0.50	N/A
dt_{max}	Maximum allowable time step	1/12 yr	N/A
D_r	Percent of water drained to aquifer	2.00%	Johnson (2002)
dt_{tun}	Time interval between tunnel checks	1/4 yr	N/A
h_c	Saturated Sediment thickness	1.00 m	Person et al. (2012)
k_a	Steepness of conductivity transition	15	Flowers et al. (2005)
k_b	Affects when conductivity transitions	0.65	Flowers et al. (2005)
K_m	Range of hydraulic conductivity	$10^{-7}-10^{-5}$	Flowers et al. (2005)
Q_{sc}	Tunnel formation condition multiplier	1.00	N/A
T_c	Basal freezing temperature below PMP	$-2.00^{\circ}C$	N/A
Z_h	Bedrock bump height	0.10 m	Kamb (1987)

Table 6.1: Chosen values for the baseline model run.

6.1 The Baseline Model

To evaluate the importance of each parameter, the model is given a baseline set of parameters. From this base set of parameters, each parameter is varied over a set of values to test how much it changes the results from the baseline results.

The value of F_{CFL} was chosen as one-half of the CFL velocity ($V_{CFL} = r\Delta\theta/\Delta t$) as a safety measure against instabilities. The value was chosen as to ensure the model is stable, as instabilities can occur below the CFL limits, but not too strict as to excessively slow down the model. The model's dynamic time stepping feature along with limiting the maximum time step, were designed with preventing those instabilities from happening. The values in the run cover values from 0.10 (strict) to 0.90 (just shy of CFL breaking).

The aquifer drainage parameter, D_r , was implemented from Johnson (2002) as a way to drain water into an aquifer. Johnson's value of D_r was 5.00%, but admittedly this value may have been too high. The value of 2.00% for D_r was chosen as the baseline value to highlight the importance of this parameter, while allowing enough water to remain so that the other parameters could be evaluated. As discussed in

section 4.8, the baseline value of 2.00% give values of aquifer drainage similar to those in Lemieux et al. (2008) for most of the ice sheet. The values for aquifer drainage testing range from no drainage to 7%, covering a 5.00% difference between baseline and maximum drainage as Johnson (2002) did in his testing of the parameter.

The other form of drainage is from the subglacial tunnels. The dt_{tun} parameter determines how often the system is checked to see if tunnel formation is allowed via eqn. 4.23. Checking for tunnels at every time step may lead to better results, but potentially at large computational expense. Testing of the dt_{tun} parameter will determine a value for dt_{tun} that provides a good balance between consistent results and computational efficiency. This parameter testing ranges from once a month up to once a year with the default at once a season.

As described in Flowers (2000), h_c is the saturated sediment layer. In simple terms it represents the sediment layer thickness multiplied by the porosity and is the saturation point of the sediment. When the basal water thickness reaches or exceeds h_c , the basal water pressure is equal to the ice overburden pressure and the ice is considered to be floating. The value for h_c can realistically change from place to place and over time as sediment deformation and ways of compacting can change. In the present model, h_c is set to a constant value in space and time and the different model runs are to test the importance of changing h_c on water flux and pressure. The range of values for this parameter is 0.10 m up to 2.00 m. The lower values were chosen in line with Flowers (2000) and Flowers et al. (2005) from Trapridge Glacier in Canada and Vatnajökul ice cap in Iceland. Rayne et al. (1996) measured the sediment layer thickness in Wisconsin, USA and found it to be up to 8.00 m thick in some places. This places value of $h_c=2.00$ m well within the range of reasonable values for an upper bound.

Along with the sediment thickness, the other important factor in Darcian water

flux is the hydraulic conductivity of the sediment. Sediment is a dilatant material that varies its conductivity based on the pressure of the water in the pore space. Hydraulic conductivity has three associated parameters (k_a , k_b , and K_m) that need to be tested. k_b controls the required water level (as a fraction of h_e) needed to begin the transition from low conductivity to higher conductivity. k_b values are allowed to run from 0.25–0.95 with the default value at 0.65. Since k_b values have to be between 0 and 1, the model tests cover a extensive range of values to test the impact that k_b has on the model results. Once the transition begins, k_a controls how quickly the conductivity increases with increasing water. k_a values ranges from 5–60 for a fourfold increase in its default value. Values beyond $k_a=60$ cause little difference to the conductivity vs. water plot from fig. 4.1, so the effects of k_a should be well captured in the model runs. K_m represents the range of hydraulic conductivity of the till, and is a combination of the maximum and minimum conductivity (K_{min} – K_{max} from section 4.4). The minimum values of the conductivity ranges from 10^{-9} – 10^{-7} m/s and the highest runs range from 10^{-5} – 10^{-3} m/s which is comparable to the values measured by Rayne et al. (1996). The tests on conductivity will determine the importance of k_a and k_b (as they cannot be directly measured), and to explore how changing the range of hydraulic conductivity affects the results. This can be used to guide researchers on the importance of accurately measuring the hydraulic conductivity of sediment.

Eqn. 4.23 determines if the water flux between cells is great enough to create a channelized flow in that area. To explore this equation further, the equation can be scaled to increase or decrease the likelihood of tunnel formation by the scaling factor Q_{sc} . By default the value of Q_{sc} is one (no enhancement to the equation) and is varied over four orders of magnitude in both directions (10^{-4} – 10^4).

As the base of the ice sheet becomes colder, the ice should begin to freeze to the bed, preventing water from flowing there. Due to the 40 km resolution of the grid,

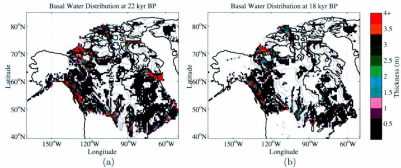
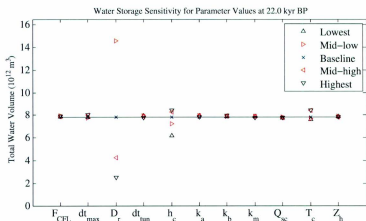


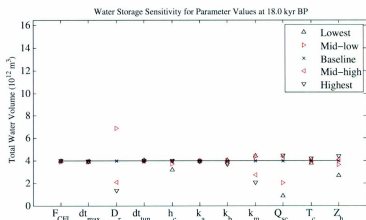
Figure 6.1: Basal water profiles for a) 22 kyr BP when the total water volume is high (mean thickness: 1.0644 ± 2.8317 m, max thickness: 86.40 m), and b) 18 kyr BP after the total water volume has drained away from the base. (mean thickness: 0.6918 ± 1.3160 m, max thickness: 24.91 m.)

it is not expected that the entire bed in a grid cell would be frozen completely. This means that water could potentially flow through a frozen cell (in the unfrozen places), but the water should have a harder time as it has less pathways to flow across. In the hydrology model, this is represented by parameter T_c , which basically acts to reduce the conductivity as a function of temperature. When the basal temperature is close to PMP there is little change to the conductivity, and it decreases to a really low value as the temperature approaches the value of T_c . In the model simulations, the value of T_c , relative to PMP, is tested from -0.5°C to -3.0°C .

In the linked cavity theory, the size of the cavity is partially controlled by the bumps at the bed. The controlling bump size, Z_h , is tested over a range of 0.01–0.50 m. This covers a range of values surrounding the standard value of 0.1 m (Kamb et al., 1985). Changing the value of Z_h affects the amount of water that can be stored and will affect the tunnel formation from eqn. 4.23.



(a)



(b)

Figure 6.2: Sensitivity plot at a) 22 kyr BP and b) 18 kyr BP. Plots show that different parameters are important at different times during the glacial cycle.

Discussion

Fig. 6.2 shows that the total basal water volume changes with varying the parameters. As a quick note, it is easy to see that the parameter F_{CFL} has little effect on the amount of water storage beneath the ice, whereas the aquifer drainage parameter significantly changes the water volume for the changes made over the range of parameter values.

For most of the other parameters, there are times when they are important and times when they are not. For example, sediment thickness, from fig.6.2, shows a larger impact at 22 kyr BP than at 18 kyr BP. This shows that the importance of a parameter depends on other factors, such as the amount of water stored in the system

Fig. 6.2a shows the model sensitivity at 22 kyr BP when the total water volume is higher in the baseline model. The most important parameter is the aquifer drainage parameter, because it simply drains a percentage of the water. This simple parameterization of the aquifer can quickly drain a lot of water as it does not have to flow to the terminus to escape and the aquifer does not return it to the ice-bed interface. In fig. 6.2b, at 18 kyr BP, the aquifer drainage is still the most important parameter, but its impact is less noticeable since there is less water to drain away from the bed.

The sediment thickness parameter (h_c) shows a 28% drop in water volume over the range of values at 22 kyr BP. At 18 kyr BP the impacts of h_c are greatly reduced and has no effect on water volume when raised above the baseline value. As explained in appendix A, this is due to the nonlinear relation between water pressure and the sediment thickness. In areas where the water level is only a small fraction of the sediment thickness, the basal water pressure will be practically zero. At 18 kyr BP, when the water level is low, an increase in sediment will have little effect on the results.

Varying the values of the basal freezing parameter, T_c , does not alter the water

storage significantly. This suggests that there is few places where the water becomes trapped beneath the ice. The runs with freezing values closer to PMP have about a 12% difference suggesting there is some water trapped due to the freezing of the ice to the bed.

The tunnel scaling factor Q_{sc} , show almost no impact in times of high water storage, but shows up to 80% drop in water volume at 18 kyr BP. During this time, the model is sensitive to Q_{sc} because the lower water levels are less likely to form tunnels than the thicker values at 22 kyr BP. Lowering Q_{sc} allows more tunnels to form, which drains the water, keeping the water volume down.

The bedrock bump height, Z_h , has a similar effect to Q_{sc} since it affects tunnel formation as well. As explained in appendix A, the larger values of Z_h allow the cavity system to retain more water before they fill up and become unstable. This allows the runs with higher Z_h to have more water as the cavities fill up.

The results of changing the range of hydraulic conductivity (K_m), show little difference in the results at higher water volumes for the different runs. However, at 18 kyr BP there is a big difference in the results. The results show that as hydraulic conductivity increases, the total water volume decreases. This is expected since increasing the conductivity increases the water flow and tunnel formation, allowing the water to evacuate from the ice sheet. The two parameters, k_a and k_b , that affect how quickly and when the switch between the low and high hydraulic conductivity regimes show little influence on the model results. This is rather fortuitous since they are not physical parameters that can be easily measured, whereas the range of conductivity can be constrained based on the type of sediment from field studies.

The results from the runs show the lack of importance of how often the model checks for tunnel formation (dt_{tun}). The reason for this lack of model sensitivity lies in the time it takes to refill the grid cell with water. If it takes a grid cell more than

a year (the largest value of dt_{tun}), then the model will not be sensitive to dt_{tun} as the frequency of tunnels will not change drastically. The effect of lowering dt_{tun} may have a minor effect on when the tunnels form, but not how often (as shown in appendix A), though this could change if larger values of dt_{tun} were used.

One pleasant result of the model runs was the insignificance of the maximum allowable time step (dt_{max}) on the results. There is only a 10% water volume drop in the range of values chosen. Also, as the time steps become smaller (the lowest value was 1/3 of the baseline value), they begin to converge to an answer somewhere in the vicinity of the baseline values. This suggests that the model shows both stability and convergence for decreasing time steps.

6.2 Effects of Varying Parameters on Basal Water Thickness

The water thickness in a grid cell underneath the ice can be sensitive to the parameter set chosen. Changing parameters may cause the water to flow at different rates, changing the type of drainage system present and affecting the basal water pressure. For example, increasing the hydraulic conductivity should be more conducive to tunnel formation, removing water from the cell, whereas increasing the sediment thickness should hinder tunnel growth due to decreased water pressure. These changes in water thickness can cause significant changes to the ice sheet dynamics as the location of water will affect the time and place of fast flowing ice. The following discussion is a quick summary of the results from the model runs, further results and discussion can be found in appendix A.

From the results in the previous section, F_{CFL} , dt_{max} , dt_{tun} , and T_c do not have much impact on the results. The results in 6.4 are for the maximum allowable time

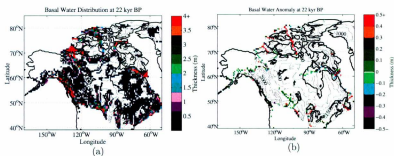


Figure 6.3: Results with maximum $dt_{max} \approx 1$ year. Basal water thickness has a mean and standard deviation of 1.0513 ± 2.6768 m with a maximum value of 86.40 m.

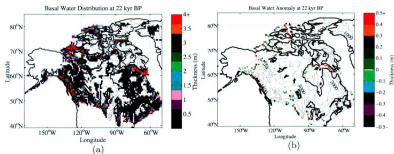


Figure 6.4: Results with $dt_{max} \approx 10$ days. Maximum basal water thickness was 86.40 m with a mean of 1.0690 ± 2.7765 m.

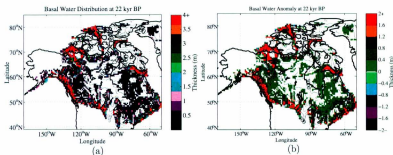


Figure 6.5: Results with $D_r=1.00\%$. The maximum basal water thickness exceeded 99.99 m and the mean thickness increased to 1.8897 ± 4.3385 m.

step, dt_{maz} , but the other parameters listed show similar results (see appendix A). Since these parameters (except T_c) are related to time steps, this suggests that the model is convergent at small time steps. T_c does not show much impact because there are few places for the water to become trapped in the GSM runs of the NAIC.

In contrast to the above parameters, the aquifer drainage parameter had the most impact on the water storage. Fig. 6.5 shows that when the amount of drainage is cut in half, the water level in each cell generally increases by 0-0.4 m. This value is higher in areas with thicker water, causing the areas where ice streaming could occur to occupy a larger area of the ice sheet. For example, the ice stream in Yukon, Canada now stretches into the Mackenzie river and the Great Bear Lake that was not present in the baseline results in fig. 6.1.

Fig. 6.6 shows how increasing the hydraulic conductivity universally decreases the water level, especially near the terminus. This is expected since increasing the hydraulic conductivity will increase the rate of Darcy flow, which will also increase the likelihood of tunnel formation. The results for smaller bed bump height and lower tunnel scaling factor (i.e., the lowest model runs for Z_h and Q_{sc}), show similar water distributions. Since Z_h and Q_{sc} only affect the likelihood of forming tunnels in

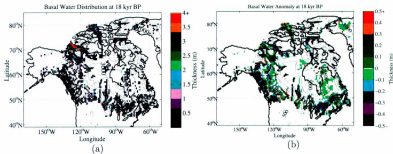


Figure 6.6: Results with the range of hydraulic conductivity $k_m = 10^{-5}-10^{-3}m/s$. With the increased hydraulic conductivity, the mean basal water thickness dropped to 0.4305 ± 1.2594 m with a maximum of 27.39 m.

eqn. 4.23, then this suggests that the main contribution to the importance of hydraulic conductivity is the increased likelihood of forming tunnels.

Changes in the saturation point of the sediment are not as prominent as changes in the hydraulic conductivity, but it does have a significant effect on the water distribution. The lowering of h_c will increase basal water pressures and fluxes, leading to more tunnel formation. The effects of h_c are most noticeable in the Hudson Bay Ice Stream, which would no longer be streaming at 22 kyr BP as it would have in the baseline run.

6.3 Identifying Areas of Fast Flow and Esker Formation

One of the aspects of the model is the ability to map out the location of areas of potentially fast flowing ice. To illustrate this point, consider the results from the baseline model run. The plots in fig. 6.8 show the effective pressure at the base of the NAIC near LGM and during its retreat. The areas with low effective pressure

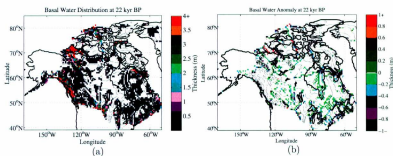


Figure 6.7: Results with $h_c=0.10$ m. While not as effective as increasing hydraulic conductivity, the lower h_c decreases the mean basal water thickness to 0.8629 ± 2.1697 m with a maximum value of 55.41 m.

(notably the red coloured areas) are where the ice would most likely be streaming due to low friction at the base. As the GSM already has parameterized ice streaming (areas with fast flowing and gentle sloping ice), the data presented in fig. 6.8, show that the areas of low effective pressure match-up with the simulated ice streams from the GSM.

Still using the baseline model run, the plots in fig. 6.9 are snapshots of the NAIC as it retreats from a nearly full ice sheet down to a much smaller LIS that is just beyond the Hudson Bay area (with the Cordillera Ice Sheet gone by 10 kyr BP). The lines in the plots show the location of subglacial tunnels at that particular moment in time. The images show that the Cordillera Ice Sheet breaks down much quicker than the LIS. All the melting of the Cordillera inputs a lot of water into the ice sheet and there are many subglacial channels surrounding the ice sheet and carrying the water away. During the retreat of the LIS, there are several tunnels formed at the edge of the ice sheet over Northern and Central Canada (the Canadian Shield). Future work will examine the extent to which tunnel prevalence in the model correlates with observed esker density (e.g., Clark and Walder (1994)).

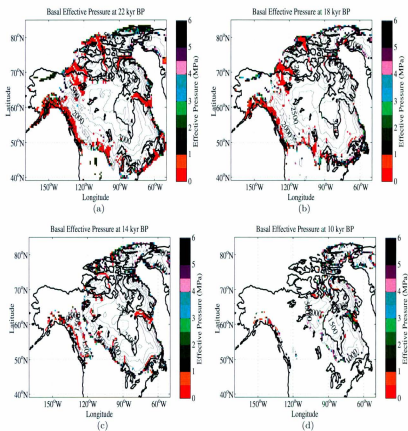


Figure 6.8: Areas with low effective pressure indicate areas of fast flowing ice.

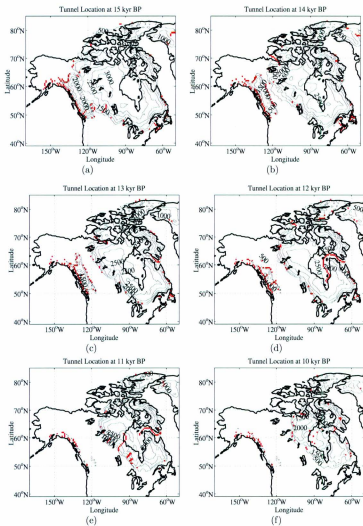


Figure 6.9: Location of tunnel formation as the LIS began to retreat.

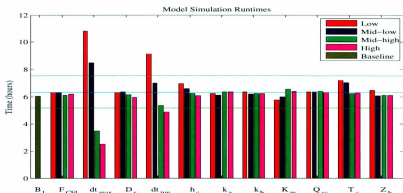


Figure 6.10: Model simulation time over 120 kyr glacial cycle for sensitivity tests. The coloured bars represent the time the model took to complete the glacial cycle as each of the model parameters on the horizontal axis was varied across their range of values. The cyan line is the mean run time and the green lines show 1 standard deviation from the mean.

6.4 Model Runtime

All the models simulations were compiled and optimized using the Fortran compiler from the Portland Group (PGF90 compiler). A series of model runs were executed on a commodity computer cluster (each run on a single processor core). On average, the model required 6 hours and 20 minutes to, with a standard deviation of 1 hour and 11 minutes, to complete a full glacial cycle for variations in the parameter set. Fig. 6.10 shows that the majority of the runs are within one standard deviation from the mean run time, showing consistency in the computational speed of the model. The worst run times were the ones that enforced a really small time step (dt_{max}) or had frequent calls to check for tunnel formation (dt_{min}). Fortunately, the model showed that using the stricter time steps and more tunnel calls did not affect the results significantly, so using these parameter sets may be avoided.

Chapter 7

Conclusion

7.1 Summary

The aim of this project is to develop a physically-based subglacial hydrology to incorporate into continental-scale glacial system model to simulate distributed and channelized systems (see chapter 2). To achieve this, the hydrology model simulates the distributed drainage system with Darcian flow, as described in Flowers (2000) and chapter 4. The channelized flow uses a down gradient solver developed in Tarasov and Peltier (2006), that flows water in the direction of lowest potential. The condition for switching between the two drainage systems is based on a critical water flux described in Schoof (2010), which is qualitatively similar to the orifice stability parameter from Kamb (1987). When the switch from Darcian flow to tunnel occurs, the down gradient solver instantaneously moves the water where it should be to minimize the potential gradients in the channelized system. From there, the channelized system is shut down and Darcian flow resumes. The model time is advanced using a combination Heun's method and Leapfrog-Trapezoidal schemes. These schemes are predictor-corrector schemes that provide the model with second-order accuracy

while maintaining stability and robustness (Mathews and Fink, 2004; Shepetchkin and McWilliams, 2005).

Simplified ice sheet and bedrock geometries are created to validate the model by comparing the results to what would be expected in those situations. The Darcy model is tested for mass conservation as it is a requirement for physically accurate results. For the first set of tests, the channelized flow is turned off and the model is run with only Darcian flow. These tests are simulated over a flat bed to see if: 1) Darcian flow has the same symmetry as the simplified ice sheet; 2) on an inclined bed to test if water would flow quicker when flowing downhill and be hindered as it flowed uphill (as the ice sheet would force this); and 3) over a dilating bed to see if water can from lakes in areas of lower hydraulic potential. The second set of validation tests has both the Darcian and channelized flow activated. These tests use the same set-ups to evaluate the impact that tunnel formation has on draining water and creating subglacial lakes.

With the validation tests complete, the model is incorporated into the MUN/UoT GSM (Tarasov and Peltier, 1999, 2002, 2004; Tarasov et al., 2012). The one-way coupling to the GSM allowed for sensitivity testing of the hydrology model to changes in the parameters in terms water volume and thickness. The model sensitivity tests determined which parameters are the most important parameters, guiding further studies to find ways to better constrain them. The results of the GSM model runs show that the GSM's simulated ice streams and the hydrology model's areas of low effective pressure align properly, as areas of ice streaming will have low basal effective pressures.

One of the key indicators of tunnel formation is the location of eskers on deglaciated beds. Since the model can also record the locations of subglacial tunnels, this will permit future detailed comparisons against observational data.

7.1.1 Summary of Model Results

- Model validation confirms
 - The Darcian component of the model conserves mass.
 - Water flows down potential gradients and is hindered somewhat by inverse bed slopes.
 - Inverse bed slopes and gentle ice slopes, can allow the water to form lakes.
 - The inclusion of channelized flow greatly reduces the amount of basal water.
 - Lakes are larger with the inclusion of channelized flow, as the lake were able to obtain more water from a wider basin than with Darcian flow alone. The relevance of this point may have more to do with the simplified aquifer used in the model (and in hind-sight a likely to strong a drainage flux into the aquifer), since the size of a lake should be mostly dependent on the hydraulic potential field.
- The results from coupling with the GSM show
 - The most sensitive model parameters are physically based.
 - In times of high water input, the most influential parameters are sediment pore space and aquifer drainage.
 - In times of lower water levels, the important parameters are related to tunnel formation, such as the bedrock bump height, tunnel scaling factor, and the hydraulic conductivity.
 - Prominent areas of low effective pressure (ideal for ice streaming) occur in the Hudson Strait, the high Canadian Arctic, along the Mackenzie River and along the coast of British Columbia, Canada.

- During deglaciation, fig. 6.9 shows tunnel formation over different areas of the Canadian Shield which may explain the vast number of eskers in the region.
- Simulations of the NAIC over a continental-scale, full glacial cycle with a grid resolution of 0.5° longitude by 1.0° latitude, took a mean time 6 hours and 20 minutes with a standard deviation of 1 hour and 11 minutes.

7.2 Future Work

As a first attempt at developing a basal hydrology model, the model works very well. Even in a one-way coupling to the GSM, the results indicate that areas with low effective pressures from the hydrology model were consistent with the areas of ice streaming in the GSM. The model has also shown itself to be rather robust and stable for a wide range of parameter values. That said, there are still some improvements that could be made to the model to further study the LIS.

7.2.1 Examine dynamics with full 2-way coupling of hydrology model with the GSM

Full coupling the hydrology model to the GSM will allow the water distribution to affect the ice sheet itself. This can have a multitude of effects on the ice sheet as certain parts undergo ice streaming as the water pressure reduces basal friction. The hydrology model can be allowed to affect the GSM via a sliding law (Huybrechts, 1992)

$$\vec{u}_b = A_* \frac{\tau_b^p}{P_{eff}^q} \quad (7.1)$$

where u_b is the basal sliding velocity, A_s is a constant inversely proportional to the bed roughness, $\bar{\tau}_b$ is the basal shear stress, p_{eff} is the effective pressure, p and q are parameters to be determined. As the basal water pressure increased, the sliding velocity, \bar{u}_b , would increase due to its inverse relationship to effective pressure.

Ice streaming can alter the shape of the ice sheet causing it to become flatter. This smoothing of the surface slope would potentially allow lakes to form near depressions as seen in the model validation in chapter 5. Faster flowing ice would expand the areal extent of the ice sheet as ice could flow into areas where the amount of ablation would not allow ice to form and would create more calving at the ice fronts as more and more ice would be pushed into those areas. The inclusion of basal hydrology would also allow the study into jökullaups and mass drainage events that could lead to changes in the climate, such as the surge of fresh water that caused the Younger Dryas.

7.2.2 Examine Sensitivity to value of Exponent in the Basal Water Pressure Equation

All the model simulations in this project followed the eqn. 4.15, which was derived from Flowers (2000). As such, eqn. 4.15 can be recast as

$$P_W = P_I \left(\frac{w}{h_e} \right)^q \quad (7.2)$$

to allow testing of the sensitivity of eqn. 4.15 to changes in the exponent.

Changing the exponent will affect how quickly the basal water pressure will increase with increased water thickness. This change in water pressure will affect the formation of channelized flow as the changes in pressure will affect the basal water flux. The changes to pressure will also affect the ice by changing the effective pressure

at the base of the ice. This, in turn, will affect the sliding velocity of ice via the basal sliding law discussed above.

7.2.3 Recast the Saturated Sediment Parameter, h_c , into a Spatially Dependent Variable

The sediment pore space in the previous test was set to constant in time and space. This is not particularly physical as sediments can undergo deformation and can be transported via plucking and entrainment into the ice. This can cause major changes to the sediment distribution beneath the ice, which makes the assumption in this model a rather crude one. One solution to this is to recast the sediment pore space into a variable based on sediment thickness and porosity and couple the hydrology model to a sediment deformation model. Currently, there is an in-house sediment deformation model (Melanson, 2012) being developed that would allow this.

The coupling of the sediment deformation and basal hydrology solvers would create a complex basal environment that could potentially enhance basal sliding. In areas of low sediment thickness there could be increased basal sliding due to increased water pressures as the reduced sediment pore space quickly fills up, and less sliding in areas of thicker sediment. There can also be increased basal sliding as the sediment may undergo increased deformation as the water trapped in the pore space will weaken the cohesive strength of the sediment, causing it break and provide the ice with a low friction base (similar to the role ball bearings in various rotating devices).

7.2.4 Develop a Physically-Based Aquifer

Due to time constraints the aquifer drainage developed in Flowers (2000) was dropped in favour of the drainage parameter of Johnson (2002), as the main goal of the project

is focused on the hydrological drainage system development and evolution. Adding the aquifer would have increased the level of complexity of the model results. The physically-based aquifer would have made analyzing the hydrology parameters more difficult, as water in the aquifer can also re-emerge in other parts of the basal system. This could give potentially give misleading results on the importance of the different parameters as they were tested over a range of values.

Analysis without the aquifer will allow a greater understanding of the importance of the aquifer in future tests with the aquifer present, as its effects on the system can be distinguished from the other parameters. Creating a dedicated aquifer drainage would allow for further testing of water drainage beneath the ice considering how important the aquifer drainage parameter was in the model validation and GSM runs. Developing aquifer physics would allow different amounts of drainage based on the type of bed, such as allowing more drainage in the sediment layer of the prairies than in the bedrock of the Canadian Shield due to their different infiltration rates (Lemieux et al., 2008). This could have a major impact on the basal water availability. If the amount of water drainage to the aquifer is reduced, then there is likely to be either more ice streaming for moderate increases in water availability and tunnel formation if the increased water levels causes fluxes in excess of the critical flux for tunnel formation. Conversely, if the aquifer drainage is increased, then there will be less ice streaming due to less basal water.

Bibliography

- Alley, R. B. (1989). Water-Pressure Coupling of Sliding and Bed Deformation : I. Water System. *Journal of Glaciology*, **35**(119):pp. 108–118.
- Alley, R. B. (1991). Deforming-bed origin for southern Laurentide till sheets? *Journal of Glaciology*, **37**(125):pp. 67–76.
- Alley, R. B. (1996). Towards a hydrological model for computerized ice-sheet simulations. *Hydrological Processes*, **10**:pp. 649–660.
- Arnold, N. and Sharp, M. (2002). Flow variability in the Scandinavian ice sheet: modelling the coupling between ice sheet flow and hydrology. *Quaternary Science Review*, **21**:pp. 485–502.
- Bartholomew, I. D., Nienow, P., Sole, A., Mair, D., Cowton, T., King, M. A., and Palmer, S. (2011). Seasonal variations in Greenland Ice Sheet motion: Inland extent and behaviour at higher elevations. *Earth and Planetary Science Letters*, **307**:pp. 271–278.
- Benn, D. I. and Evans, D. J. A. (2010). *Glaciers and Glaciation*. Hodder Education, London, 2nd edition.
- Björnsson, H. (1998). Hydrological characteristics of the drainage system beneath a surging glacier. *Nature*, **395**:pp. 771–774.

- Boulton, G. S. and Jones, A. S. (1979). Stability of temperate ice caps and ice sheets resting on beds of deformable sediments. *Journal of Glaciology*, **24**(90):pp. 29–43.
- Boulton, G. S., Lunn, R., Vidstrand, P., and Zatsepin, S. (2007). Subglacial drainage by groundwater-channel coupling, and the origin of esker systems: Part 1—glaciological observation. *Quaternary Science Reviews*.
- Brennand, T. A. (2000). Deglacial meltwater drainage and glaciodynamics: inferences from Laurentide eskers, Canada. *Geomorphology*, **32**(3-4):pp. 263–293.
- Carter, S. P., Blankenship, D. D., Young, D. A., Peters, M. E., Holt, J. W., and Siegert, M. J. (2009). Dynamic Distributed Drainage Implied by the Flow Evolution of the 1996-1998 Adventure Trench Subglacial Lake Discharge. *Earth and Planetary Science Letters*, **283**:pp. 24–37.
- Clark, P. U. and Walder, J. S. (1994). Subglacial drainage, eskers, and deforming beds beneath the Laurentide and Eurasian ice sheets. *Geological Society of America Bulletin*, pp. 304–314.
- Creys, T. T. and Schoof, C. G. (2009). Drainage through subglacial water sheets. *Journal of Geophysical Research*, **114**. F04008.
- Dansgaard, W., Johnsen, S. J., Clausen, H. B., Dahl-Jensen, D., Gundestrup, N. S., Hammer, C. U., Hvidberg, C. S., Steffensen, J. P., Sveinbjörnsdóttir, A. E., Jouzel, J., and Bond, G. (1993). Evidence for general instability of past climate from a 250-kyr ice-core record. *Nature*, **364**:pp. 218–220.
- Evatt, G. W., Fowler, A. C., Clark, C. D., and Hulton, N. R. J. (2009). Subglacial floods beneath ice sheets. *Philosophical Transactions of the Royal Society A*, **364**:pp. 1769–1794.

- Flowers, G. E. (2000). *A multicomponent coupled model of glacier hydrology*. Ph.D. thesis, The University of British Columbia.
- Flowers, G. E., Björnsson, H., Pálsson, F., and Clarke, G. K. C. (2004). A coupled sheet-conduit mechanism for jökulhlaup propagation. *Geophysical Research Letters*, **31**. L05401.
- Flowers, G. E. and Clarke, G. K. C. (2002). A multicomponent coupled model of glacier hydrology 1. Theory and synthetic examples. *Journal of Geophysical Research*, **107**(B11). 2287.
- Flowers, G. E., Marshall, S., Björnsson, H., and Clarke, G. K. C. (2005). Sensitivity of Vatnajökull ice cap hydrology and dynamics to climate warming over the next 2 centuries. *Journal of Geophysical Research*, **110**.
- Fountain, A. G. and Walder, J. S. (1998). Water flow through temperate glaciers. *Reviews of Geophysics*, **36**(3):pp. 299–328.
- Fowler, A. C. (1987). Sliding with cavity formation. *Journal of Glaciology*, **33**(115):pp. 255–267.
- Fowler, A. C. and Larsen, D. A. (2010). On the flow of polythermal glaciers. *Proceedings of the Royal Society London A*, **363**:pp. 217–242.
- Glen, J. (1955). The creep of polycrystalline ice. *Proceedings of the Royal Society of London*, **228**(1175):pp. 519–538.
- Heinrich, H. (1988). Origin and Consequences of Cyclic Ice Rafting in the Northeast Atlantic Ocean during the Past 130,000 Years. *Quaternary Research*, **29**:pp. 142–152.

- Hindmarsh, R. C. A. and Payne, A. J. (1996). Time-step limits for stable solutions of the ice sheet equation. *Annals of Glaciology*, **23**:pp. 74–85.
- Hooke, R. L. and Fastook, J. (2007). Thermal conditions at the bed of the Laurentide ice sheet in Maine during deglaciation: implications for esker formation. *Journal of Glaciology*, **53**(183):pp. 646–658.
- Huybrechts, P. (1992). *The Antarctic ice sheet and environmental change: a three-dimensional modelling study*, chapter 4. Reports on Polar Research. Alfred Wegener institute for Polar and Marine Research, Bremerhaven.
- IPCC (2007). *Climate Change 2007: Synthesis Report. Contribution of Working Groups I, II and III to the Fourth Assessment Report of the Intergovernmental Panel on Climate Change*. [Core Writing Team, Pachauri, R.K and Reisinger, A. (eds.)]. IPCC, Geneva, Switzerland, 104 pp.
- Johnson, J. and Fastook, J. L. (2002). Northern Hemisphere glaciation and its sensitivity to basal melt water. *Quaternary International*, **95-96**:pp. 65–74.
- Johnson, J. V. (2002). *A Basal Water Model for Ice Sheets. Doctorate Thesis Abstract*. Ph.D. thesis, The University of Maine.
- Kamb, B. (1987). Glacier surge mechanism based on linked-cavity configuration of basal water conduit system. *Journal of Geophysical Research*, **92**(B9):pp. 9083–9100.
- Kamb, B., Engelhardt, H., Fahnestock, M. A., Humphrey, N., Meier, M., and Stone, D. (1994). Mechanical and hydrologic basis for the rapid motion of a large tidewater glacier 2. Interpretation. *Journal of Geophysical Research*, **99**(B8):pp. 15231–15244.

- Kamb, B., Raymond, C. F., Harrison, W. D., Engelhardt, H., Echelmeyer, K. A., Humphrey, N., Brugman, M. M., and Pfeffer, T. (1985). Glacier Surge Mechanism: 1982-1983 Surge of Variegated Glacier, Alaska. *Science*, **227**(4686):pp. 469-479.
- Lemieux, J. M., Sudicky, E. A., Peltier, W. R., and Tarasov, L. (2008). Dynamics of groundwater recharge and seepage over the Canadian landscape during the Wisconsinian glaciation. *Journal of Geophysical Research*, **113**:pp. 1-18. F01011.
- Liboutry, L. (1987). Sliding of cold ice sheets. In *The Physical Basis of Ice Sheet Modelling (Proceedings of the Vancouver Symposium, August 1987)*, volume 170, pp. 131-143. IAHS Publ.
- Marshall, S. J. (1996). *Modelling Laurentide Ice Stream Thermomechanics*. Ph.D. thesis, University of British Columbia.
- Mathews, J. H. and Fink, K. K. (2004). *Numerical Methods Using Matlab*, chapter 9. Prentice-Hall Inc., 4th edition.
- Melanson, A. (2012). Numerical modelling of subglacial erosion and sediment transport and its application to the North American ice sheets over the last glacial cycle. Unpublished masters thesis, Memorial University of Newfoundland, St. John's, Canada.
- Murray, T. and Porter, P. R. (2001). Basal conditions beneath a soft-bedded polythermal surge-type glacier: Bakaninbreen, Svalbard. *Quaternary International*, **86**:pp. 103-116.
- Nerem, R. S. and Wahr, J. (2011). Recent changes in the Earth's oblateness driven by Greenland and Antarctic ice mass loss. *Geophysical Research Letters*, **38**. L13501.

- Nye, J. F. (1967). Theory of Regelation. *Philosophical Magazine*, **16**(144):pp. 1249–1266.
- Nye, J. F. (1976). Water Flow in Glaciers: Jökulhlaups, Tunnels and Veins. *Journal of Glaciology*, **17**(76):pp. 181–207.
- Patankar, S. V. (1980). *Numerical Heat Transfer and Fluid Flow*. Series in computational methods in mechanics and thermal sciences. Hemisphere Publishing Corporation, Washington.
- Paterson, W. S. B. (1981). *The Physics of Glaciers*. Elsevier Science Ltd., Great Britain, 2nd edition.
- Payne, A. J., Huybrechts, P., Abe-Ouchi, A., Calov, R., Fastook, J. L., Greve, R., Marshall, S. J., Marsiat, I., Ritz, C., Tarasov, L., and Thomassen, M. P. A. (2000). Results from the EISMINT model intercomparison: the effects of Thermomechanical coupling. *Journal of Glaciology*, **46**(153):pp. 227–238.
- Person, M., Bense, V., Cohen, D., and Banerjee, A. (2012). Models of ice-sheet hydrogeologic interactions: a review. *Geofluids*, **12**(1):pp. 58–78.
- Rayne, T., Bradbury, K., Mickelson, D., and Wisconsin Geological and Natural History Survey (1996). *Variability of hydraulic conductivity in uniform sandy till, Dane County, Wisconsin*, volume 74 of *Information Circular*. Wisconsin Geological and Natural History Survey.
- Röthlisberger, H. (1972). Water Pressure in Intra- and Subglacial Channels. *Journal of Glaciology*, **11**(62):pp. 177–203.
- Schoof, C. (2010). Ice-sheet acceleration driven by melt supply variability. *Nature*, **468**:pp. 803–806.

- Shchepetkin, A. F. and McWilliams, J. C. (2005). The regional oceanic modeling system (ROMS): a split-explicit, free-surface, topography-following-coordinate oceanic model. *Ocean Modelling*, **9**:pp. 347–404.
- Stewart, R. H. (2005). Introduction to Physical Oceanography. Retrieved from http://oceanworld.tamu.edu/resources/ocng_textbook/contents.html.
- Tarasov, L., Dyke, A. S., Neal, R. M., and Peltier, W. R. (2012). A data-calibrated distribution of deglacial chronologies for the North American ice complex from glaciological modeling. *Earth and Planetary Science Letters*, pp. 1–29.
- Tarasov, L. and Peltier, W. R. (1997). Terminating the 100 kyr ice age cycle. *Journal of Geophysical Research*, **102**(D18):pp. 21,665–21,693.
- Tarasov, L. and Peltier, W. R. (1999). Impact of Thermomechanical ice sheet coupling on a model of the 100 kyr ice age cycle. *Journal of Geophysical Research*, **104**(D8):pp. 9517–9545.
- Tarasov, L. and Peltier, W. R. (2002). Greenland glacial history and local geodynamic consequences. *Geophys. J. Int.*, **150**:pp. 198–229.
- Tarasov, L. and Peltier, W. R. (2004). A Geophysically constrained large ensemble analysis of the deglacial history of the North American ice-sheet complex. *Quaternary Science Review*, **23**:pp. 359–388.
- Tarasov, L. and Peltier, W. R. (2006). A calibrated deglacial drainage chronology for the North American continent: evidence of an Arctic trigger for the Younger Dryas. *Quaternary Science Review*, **25**:pp. 659–688.
- Walder, J. S. (1982). Stability of Sheet Flow of Water Beneath Temperate Glaciers and Implications for Glacier Surging. *Journal of Glaciology*, **28**(99):pp. 273–293.

- Walder, J. S. (1986). Hydraulics of subglacial cavities. *Journal of Glaciology*, **32**(112):pp. 439–445.
- Walder, J. S. and Fowler, A. C. (1994). Channelised subglacial drainage over a deformable bed. *Journal of Glaciology*, **40**(134):pp. 3–15.
- Walder, J. S. and Hallet, B. (1979). Geometry of former subglacial water channels and cavities. *Journal of Glaciology*, **23**(89):pp. 335–346.
- Weertman, J. (1972). General theory of water flow at the base of a glacier or ice sheet. *Reviews of Geophysics and Space Physics*, **10**(1):pp. 287–333.
- Weertman, J. (1974). Stability of the junction of an ice sheet and an ice shelf. *Journal of Glaciology*, **13**(67):pp. 3–11.
- Weertman, J. and Birchfield, G. E. (1983a). Basal water film, basal water pressure, and velocity of traveling waves on glaciers. *Journal of Glaciology*, **29**(101):pp. 20–27.
- Weertman, J. and Birchfield, G. E. (1983b). Stability of Sheet Water Flow Under a Glacier. *Journal of Glaciology*, **29**(103):pp. 374–382.
- Williams, G. (1970). Manning formula—a misnomer? *Journal of the Hydraulics Division, American Society of Civil Engineers*, **96**(HY 1):pp. 193–200.
- Zevenbergen, L. W. and Thorne, C. R. (1987). Quantitative Analysis of Land Surface Topography. *Earth Processes and Landforms*, **12**:pp. 47–56.

Appendix A

One-way Coupling of the Hydrology Model to the GSM: In-Depth Analysis

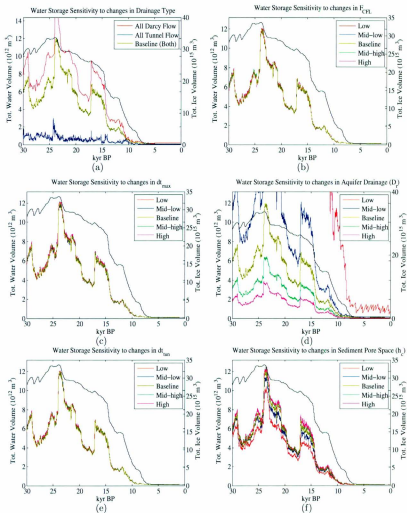
A.1 Parameter Impacts on Basal Water Storage

Discussion

During Times of Increased Water Volumes

Fig. A.1 shows the model sensitivity up to 30 kyr BP (before this time there is not much water present, much like the last 10 kyr BP). Similar to the plots in fig. 6.2, fig A.1 shows the model sensitivity to the various parameters. Fig A.1 re-enforces the idea presented in chapter 6, that the importance of a parameter depends on the amount of water present. The following discussion is not as complete as chapter 6, but rather provides some extra details about the parameters h_c and Z_h .

Changing h_c shows a 28% drop in water volume from the highest parameter value



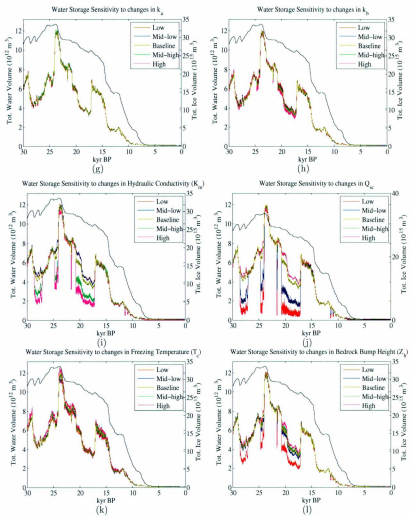


Figure A.1: Time series plot showing how model sensitivity to varying parameters changes over time.

to the lowest at 22 kyr BP. The importance of sediment thickness lies in its nonlinear effects on water pressure and hydraulic conductivity. In eqn. 4.15, the water pressure is inversely proportional to $h_c^{7/2}$. So until the water thickness approaches h_c , the water pressure will remain quite low and then rapidly increase as water thickness increases and fills up the available sediment pore space. Also, eqn. 4.14 shows that hydraulic conductivity has an inverse relation to the sediment thickness as well. As the water thickness approaches h_c , the hydraulic conductivity will tend toward the higher values due to the opening of the pores from the water forcing it open. The runs with lower sediment thickness have less water storage capacity, which leads to faster flowing water due to higher water pressures and increased conductivity. This increased flow gives rise to more tunnels forming and draining the water, leading to less water beneath the ice. In the runs with higher sediment thickness, the opposite effect occurs leading to decreased water flow and tunnel formation. After the water has drained, the results show that h_c is not so important at lower water volumes. This lies in the fact that at low water volumes, the basal water pressure is going to be very low for any moderate value for sediment thickness due to the highly nonlinear pressure equation (as a rule of thumb, if $h_c \geq 4w$ then there is relatively no change in basal water pressure).

The bedrock bump height (cavity step height) shows little influence during 22 kyr BP when the water volume is higher, but becomes significant afterwards when the water volume is lower. In the theory of linked-cavities, the size of the cavity is proportional to the size of the bedrock bumps. At 22 kyr BP, there is probably more water than the cavities can store which leads to the tunnel formation. The effectiveness of the cavities are diminished as the tunnels start to take over leading to the bedrock bumps becoming insignificant. After the water levels drop and they start to build up again, the bump size becomes important as it affects how much storage the cavities have before they fill up and become unstable (i.e., form tunnels).

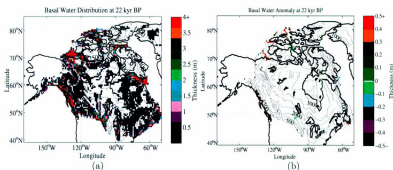


Figure A.2: Results with $F_{CFL}=0.9$. Mean water thickness: 1.06 ± 2.72 m, maximum water thickness: 86.40 m.

Numerically the bump parameter, Z_h is used in eqn. 4.23 to increase the critical water flux needed for tunnel formation as the bump size increases.

A.2 Effects of Varying Parameters on Basal Water Distribution

The following figures show the results of some of the runs along with anomaly plots that show their deviation from the baseline model from fig. 6.1.

Results

Fig. A.2b shows the difference between the baseline model ($F_{CFL}=0.5$) and the run with $F_{CFL}=0.9$. As suggested by fig. A.1, changing F_{CFL} does not have much impact on the final results. The few places where the results differ are near the edges of the ice sheet where the water builds up (e.g., the Hudson Strait and up in the Canadian Arctic) or in a few streams. Seeing as F_{CFL} causes a change in the time steps when the water flow becomes too fast, there is expected to be a slight change in the results.

So if the model is ran at even smaller time steps, the effects of F_{CFL} should decrease since the model should converge and with smaller time steps it is less likely the CFL condition would be n. This result suggests that the model time steps may be sufficiently small and converging since the impact of F_{CFL} is small.

The result of setting the maximum allowable time step to $dt \approx 1$ year is shown in fig. A.3. In comparison to the baseline run ($dt \approx 1$ month), there is a greater difference than from changing F_{CFL} . Much like F_{CFL} , most of the change occurs in the areas of water build up in the Hudson and Canadian Arctic, but there are some differences in the interior that could affect ice dynamics.

Using a smaller value ($dt \approx 10$ days) shows a much smaller difference in fig. A.4, indicating the solution is beginning to converge. So while the model does not reach complete convergence at weekly time steps, this can be expected since the original model from Flowers et al. (2005) was ran at a constant $dt=600$ s. Since this value may not be viable for continental scale modelling (though the model would probably only take a day), using a value of 10 days or 1 month do not change the results that much and are shown in section 6.4 to be viable time steps for modelling over these spatial and temporal scales.

As already stated, the aquifer drainage parameter has the most significant impact on water volume beneath the ice. In fig. A.5 shows that dropping D_r from 2.00% to 1.00% shows a huge increase in water present at the base. The most noticeable areas of water thickness from the baseline results are the Hudson Strait, the Western Cordillera, above the Yukon Territories, Canada (The Mackenzie River). Also, the two passages in the Arctic would also be at ice flotation, even though they have much less water. In fig. A.5, The large increase in water will cause the sediment to become completely saturated (water thickness greater than $h_c=1$ m for baseline results) and raise the water pressure to ice overburden pressure. In this scenario the two passages

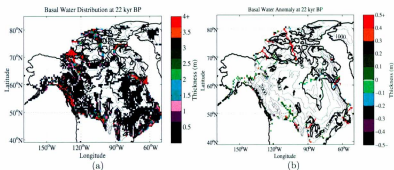


Figure A.3: Results with maximum $dt \approx 1$ year. Mean water thickness: 1.06 ± 2.72 m, maximum water thickness: 86.40 m.

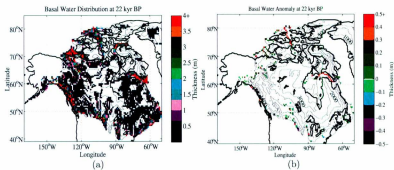


Figure A.4: Results with $dt \approx 10$ days. Mean water thickness: 1.06 ± 2.72 m, maximum water thickness: 86.40 m.

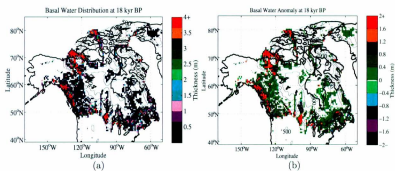


Figure A.5: Results with $D_r=1.00\%$. Mean water thickness: 1.18 ± 2.18 m, maximum water thickness: 27.20 m.

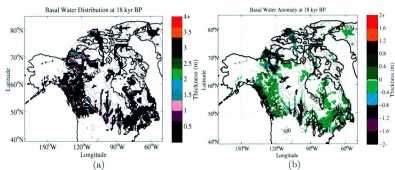


Figure A.6: Results with $D_r=4.00\%$. Mean water thickness: 0.37 ± 0.69 m, maximum water thickness: 14.67 m.

in the Arctic have a lot more water suggesting that the ice may surge longer than the baseline result. The areas that were surging in the baseline result have expanded which would have a impact on ice dynamics as more ice could flow to the margins and start calving, leading to a more flat-shaped ice sheet.

Conversely, when D_r is increased to 4.00% the results from fig. A.6 show a big drop in water volume. In this scenario, the total area of saturated sediment (i.e., where the water pressure is at ice overburden pressure) is greatly reduced. The size of the noticeable areas from the baseline are shrunk closer the edges of the ice sheet. Also the water along the Canada-USA border would no longer be at ice flotation pressure with the increased drainage. This decrease in the water volume means that the ice is less likely to be surging for long periods of time in the more noticeable areas and that certain other areas may not get to surge at all. The net effect of this should be less ice calving at the terminus, resulting in a more dome-shaped ice sheet.

figures A.7 and A.8 show the effects of varying how often tunnels are checked for, and how they differ from the baseline model. In either case, for the GSM the results still show very little change. The mostly cause of these changes is the timing of the tunnel formation. The anomaly plot for $dt_{tun}=1$ month shows that it is somewhat closer to the baseline result than the model run with $dt_{tun}=1$ year. As mentioned above, the importance of dt_{tun} depends on how quickly the water builds up in a grid cell.

Fig. A.9 shows the water distribution and anomalies at 22 kyr, when there was more water and h_c had a greater effect, and at 18 kyr, when there was less water and h_c was less influential. At 22 kyr BP, there are many spots that are slightly different from the baseline result, but the major difference occurs in the streams of the Arctic. The baseline run ($h_c=1.00$ m) has much more water in the streams than the run with $h_c=0.10$ m. The low water volume of 18 kyr BP shows that the two runs are much

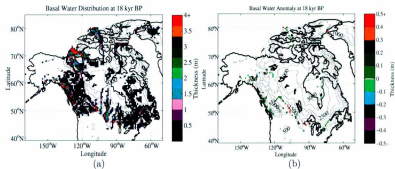


Figure A.7: Results with $dt_{\text{run}}=1$ month. Mean water thickness: 0.71 ± 1.32 m, maximum water thickness: 24.93 m.

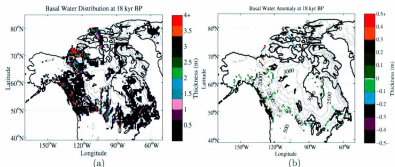


Figure A.8: Results with $dt_{\text{run}}=1$ year. Mean water thickness: 0.67 ± 1.29 m, maximum water thickness: 24.12 m.

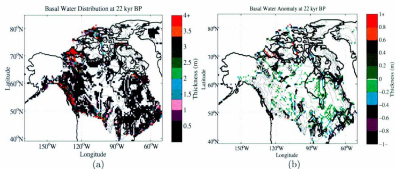


Figure A.9: Results with $h_c=0.10$ m. Mean water thickness: 0.86 ± 2.17 m, maximum water thickness: 55.41 m.

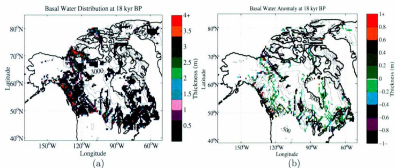


Figure A.10: Results with $h_c=0.10$ m. Mean water thickness: 0.5718 ± 1.31 m, maximum water thickness: 23.61 m.

closer than at 22 kyr BP. These results show the importance of h_c on water transport and storage in the ice streams. With thicker sediment, the increased storage powers the water pressure, hindering tunnel formation and trapping the water in the streams. The lowered pressure water can affect the ice streams by slowing them down, but they may be able to flow for longer periods of time if the water does not form a tunnel to drain.

By 18 kyr BP, the tunnels have formed and drained a lot of water from beneath the ice, and the drainage system is building up water. With the lower value of sediment thickness, the capacity of the drainage system is smaller and can be filled up quicker. In the anomaly plot in fig. A.10, there are areas (e.g., the Arctic and Central Canada) that suggest that tunnel formation has occurred in the low sediment thickness run that have not occurred in the baseline run with thicker sediment. Overall, the lower sediment thickness should create a basal system with higher water pressures, more tunnel formation, and lead to faster flowing ice velocities.

The results from fig. A.11 and A.12 suggests that the value chosen for the transition factor of the hydraulic conductivity is not overly important. The results do show that k_a can have an effect on timing of tunnel formation as indicated by the increased water thickness in the Arctic in fig. A.12. The effectiveness of k_a will depend on the range of hydraulic conductivity. For a range of two orders of magnitude in the conductivity range the changes in k_a are rather minimal, but this may be different with bigger ranges on the conductivity.

Figures A.13 and A.14 show that, much like k_a , the parameter k_b has little impact on the results. Much like k_a , k_b has a huge effect on determining the hydraulic conductivity of the drainage system. Since $k_b \times h_c$ essentially determines the water thickness at which the hydraulic conductivity starts to switch from low to high values, then the low run of k_b should switch at 0.25 m and the highest run at 0.95 m. From

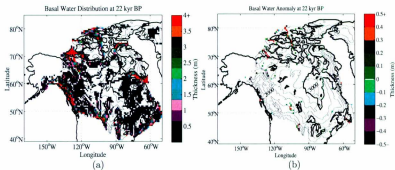


Figure A.11: Results with $k_a=5$. Mean water thickness: 1.07 ± 2.72 m, maximum water thickness: 86.40 m.

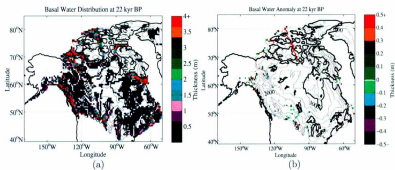


Figure A.12: Results with $k_a=60$. Mean water thickness: 1.06 ± 2.70 m, maximum water thickness: 86.40 m.

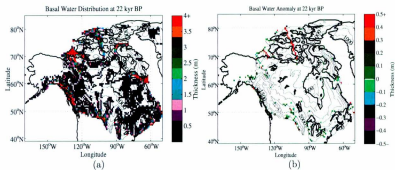


Figure A.13: Results with $k_0=0.25$. Mean water thickness: 1.07 ± 2.72 m, maximum water thickness: 86.40 m.

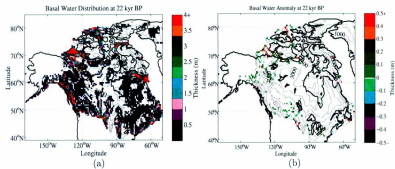


Figure A.14: Results with $k_0=0.95$. Mean water thickness: 1.07 ± 2.72 m, maximum water thickness: 86.40 m.

fig. A.13 and A.14 the distribution of water shows there are very few places where the water thickness is from 0.33–1.33 m. This shows that there are very few places where the water would be in the transition zone, so the effectiveness of k_b is diminished. This could explain the ineffectiveness of k_a , since the water needs to be transitioning for k_a to be effective as well.

As expected the hydraulic conductivity of the sediment plays an important role in the transport of basal water. The results in fig. A.1 show that model is more sensitive to the hydraulic conductivity at 18 kyr BP than at 22 kyr BP. It also shows that the conductivity is not too important at 22 kyr BP in terms of total water. Expanding on those results, fig. A.16 does show that there is a much greater difference in the results from the baseline at 18 kyr BP. At 18 kyr BP there is a much greater differences in basal water along the edges of the ice sheet than in the interior. This can be expected since there would be greater hydraulic potential gradients as the ice begins to slope more toward the edges, leading to faster Darcian flow and more tunnel formation in those areas. An increase in hydraulic conductivity will have a big impact on ice dynamics as it will lead to greater drainage at the base, resulting in slower ice and less ice streaming as the drainage at the base becomes more efficient.

In fig. A.17 the condition for tunnel formation was lowered by a factor of 100 (easier tunnel formation). The results in fig. A.17 are similar to the increased hydraulic conductivity in fig. A.16, suggesting the main influence of increasing hydraulic conductivity does come from increased tunnel formation and not so much from faster Darcian flow. As in the case of increased conductivity, lowering the requirements for tunnel formation will increase the number of tunnels and lead to slower basal sliding of the ice. When the condition is increased by a factor of 100, the results are more similar to the baseline model, suggesting there was not many tunnels occurring. There are a few places where the water is thicker than the baseline results, possibly do to

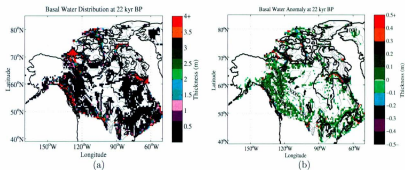


Figure A.15: Results with $k_m = 10^{-5}-10^{-3}m/s$. Mean water thickness: 1.01 ± 2.65 m, maximum water thickness: 85.45 m.

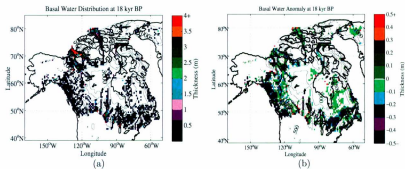


Figure A.16: Results with $k_m = 10^{-5}-10^{-3}m/s$. Mean water thickness: 0.43 ± 1.26 m, maximum water thickness: 27.39 m.

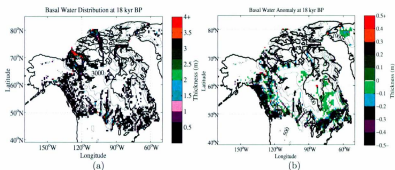


Figure A.17: Results with $Qc = 10^{-2}$. Mean water thickness: 0.44 ± 1.30 m, maximum water thickness: 27.40 m.

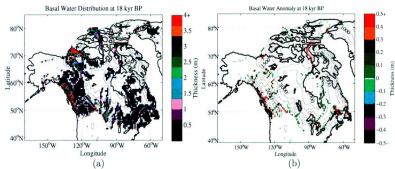


Figure A.18: Results with $Qc = 10^2$. Mean water thickness: 0.79 ± 1.77 m, maximum water thickness: 53.65 m.

the higher requirements stopping the tunnel from forming. In contrast to lowering the tunnel formation condition, making the condition higher should allow more water to stay in the drainage system, creating an ice sheet with more basal sliding.

The second way to control the hydraulic conductivity is by allowing the base of the ice to become frozen and have a much lower conductivity. The results of raising the freezing temperature from -2.0°C below PMP (baseline) to -0.5°C below PMP, as shown in fig. A.19, has a few areas where the water becomes trapped. When the freezing condition is lowered to -3.0°C below PMP, there is less freezing at the base and more water is able to escape in the Hudson Bay. The effect that T_c can have is that it can confine water in a place or cause it to find an alternative route to evacuate. If the water cannot find an alternative route then the water can become trapped and form a lake in a place that is not the lowest potential (i.e., an ice-dammed lake), which would cause the ice overhead to flow faster and flatten out.

Tunnel formation is proportional to the size of the cavities. The larger the cavity, the more water that can be stored in the cavity before it causes the connecting orifices to become unstable and form into tunnels. Since increasing the bedrock bump height (Z_h) increases the size of the cavities, then for larger Z_h there should be more water and less tunnel formation at the base. In fig. A.22, with Z_h increased five-fold to $Z_h=0.50$ m, there is not too much change from the baseline results ($Z_h=0.10$ m). The figure shows a few places where the water is thicker (e.g., the Arctic, one in Southern Quebec, and a couple of places in British Columbia), possibly due to decreased tunnel formation as the orifices are less likely to become unstable. Conversely, when Z_h is dropped to 0.05m, there is less cavity storage and more tunnel formation. This can be seen by the overall decrease in water volume in fig. A.21 and its similarities to the increase of the tunnel factor in fig. A.18.

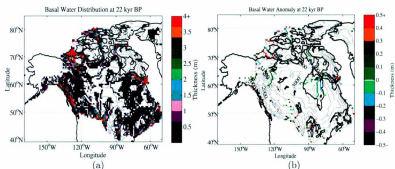


Figure A.19: Results with $T_e = 0.5^\circ C$ below PMP. Mean water thickness: 1.00 ± 2.32 m, maximum water thickness: 52.59 m.

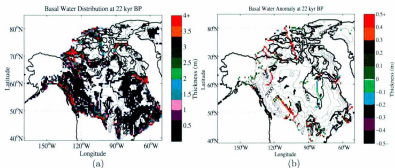


Figure A.20: Results with $T_e = 3.0^\circ C$ below PMP. Mean water thickness: 1.08 ± 2.70 m, maximum water thickness: 86.40 m.

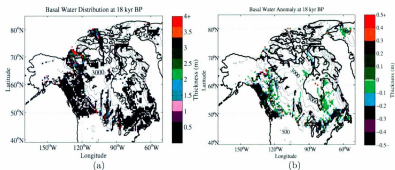


Figure A.21: Results with $Z_h = 0.05m$. Mean water thickness: 0.49 ± 1.24 m, maximum water thickness: 27.44 m.

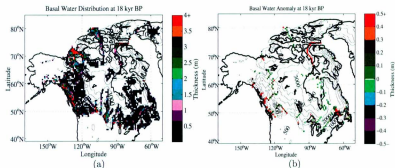


Figure A.22: Results with $Z_h = 0.50m$. Mean water thickness: 0.77 ± 1.78 m, maximum water thickness: 53.65 m.

Appendix B

Discretization of the Basal Hydrology Model

B.1 Applying Approximations to the Mass Balance Equation

Starting with eqn. 4.5 (rewritten here for convenience)

$$\iint \frac{\partial w_P}{\partial t} dV_P = \int_n^s \{Q_w - Q_e\} r d\theta + \int_e^w \{Q_s \cos \theta_s - Q_n \cos \theta_n\} r d\phi \quad (\text{B.1})$$
$$+ \iint \{b_s + b_{zb} + d_{sa}\} dV_P$$

If the model grid does not change over time, as is the case, then the time derivative can come outside the integral of the first term

$$\frac{\partial}{\partial t} \left\{ \iint w_P dV_P \right\} = \int_n^s \{Q_w - Q_e\} r d\theta + \int_e^w \{Q_s \cos \theta_s - Q_n \cos \theta_n\} r d\phi \quad (\text{B.2})$$
$$+ \iint \{b_s + b_{zb} + d_{sa}\} dV_P$$

multiplying all the terms by $\frac{1}{V_P}$

$$\frac{\partial}{\partial t} \left\{ \frac{1}{V_P} \iint w_P dV_P \right\} = \frac{1}{V_P} \int_n^s \{Q_w - Q_e\} r d\theta + \frac{1}{V_P} \iint \{ \dot{b}_s + b_{zb} + d_{sa} \} dV_P \quad (\text{B.3})$$

$$+ \frac{1}{V_P} \int_e^w \{Q_s \cos \theta_s - Q_n \cos \theta_n\} r d\phi$$

using the integral definition of the average $\bar{F} = \frac{1}{V_P} \iint F dV_P$

$$\frac{\partial \bar{w}_P}{\partial t} = \frac{1}{V_P} \int_n^s \{Q_w - Q_e\} r d\theta + \frac{1}{V_P} \int_e^w \{Q_s \cos \theta_s - Q_n \cos \theta_n\} r d\phi + \overline{\dot{b}_s + b_{zb} + d_{sa}} \quad (\text{B.4})$$

where \bar{w}_P represents the average value of water thickness over the control volume, and likewise for the source terms.

As an approximation to the real solution, it shall be assumed that Q_s and Q_n do not vary with ϕ within a grid cell, and similarly, Q_w and Q_e do not vary with θ within the grid cell (i.e., the value of the water flux is constant along any wall of the grid cell). Which leads to

$$\frac{\partial \bar{w}_P}{\partial t} = \frac{1}{V_P} \{Q_w - Q_e\} r \Delta\theta + \frac{1}{V_P} \{Q_s \cos \theta_s - Q_n \cos \theta_n\} r \Delta\phi + \overline{\dot{b}_s + b_{zb} + d_{sa}} \quad (\text{B.5})$$

the volume element V_P will be approximated by $V_P = r^2 \cos \theta_P \Delta\phi \Delta\theta$. Rewriting eqn. B.5 gives

$$\frac{\partial w_P}{\partial t} = \frac{1}{r \cos \theta_P \Delta\phi} \{Q_w - Q_e\} + \frac{1}{r \cos \theta_P \Delta\theta} \{Q_s \cos \theta_s - Q_n \cos \theta_n\} + \dot{b}_s + b_{zb} + d_{sa} \quad (\text{B.6})$$

where the average-value bars have been dropped for clarity and convenience.

B.2 Discretizing the Darcian Water Flux

Starting with eqn. 4.11, expanding the gradient gives

$$\bar{Q} = -\frac{Kw}{\rho_w g r \cos \theta} \frac{\partial(P + \rho_w g z_b)}{\partial \phi} \hat{\phi} - \frac{Kw}{\rho_w g r} \frac{\partial(P + \rho_w g z_b)}{\partial \theta} \hat{\theta} \quad (\text{B.7})$$

Looking at the flux on the westward edge of a grid cell, Q_w , we get

$$Q_w = \frac{Kw}{\rho_w g r \cos(\theta_P)} \frac{P_W - P_P + \rho_w g(z_{b_W} - z_{b_P})}{\Delta \phi} \quad (\text{B.8})$$

where the W subscript indicates the value of the grid point to the west of the central point, and the P subscript represents the centre grid cell. Using the upwind scheme from Patankar (1980)

$$Q_w = \frac{K}{\rho_w g r \cos(\theta_P) \Delta \phi} \left[\begin{aligned} & \max\{w_W[P_W - P_P + \rho_w g(z_{b_W} - z_{b_P})], 0\} \\ & - \max\{-w_P[P_W - P_P + \rho_w g(z_{b_W} - z_{b_P})], 0\} \end{aligned} \right] \quad (\text{B.9})$$

such that Q_w is positively defined if water flows eastward into the centre grid cell. Following Patankar (1980), the interface conductivity is set to the harmonic mean of the hydraulic conductivity at the two grid points

$$Q_w = \left(\frac{2K_W K_P}{K_W + K_P} \right) \left(\frac{1}{\rho_w g r \cos(\theta_P) \Delta \phi} \right) \left[\begin{aligned} & \max\{w_W[P_W - P_P + \rho_w g(z_{b_W} - z_{b_P})], 0\} \\ & - \max\{-w_P[P_W - P_P + \rho_w g(z_{b_W} - z_{b_P})], 0\} \end{aligned} \right] \quad (\text{B.10})$$

B.3 Summary of Discretized Equations Used in Hydrology Model

B.3.1 The Mass Balance Equation

Heun's Method

Euler forward (predictor) scheme

$$w_P^{1*} = w_P^0 + \frac{\Delta t}{r \cos \theta_P \Delta \phi} \{Q_w^0 - Q_e^0\} + \frac{\Delta t}{r \cos \theta_P \Delta \theta} \{Q_s^0 \cos \theta_s - Q_n^0 \cos \theta_n\} + (\dot{b}_s^0 + \dot{b}_{sb}^0 + d_{san}^0) \Delta t \quad (\text{B.11})$$

Trapezoidal (corrector) scheme

$$w_P^1 = w_P^0 + \frac{\Delta t}{2r \cos \theta_P} \left\{ \frac{Q_w^0 - Q_e^0}{\Delta \phi} + \frac{Q_s^0 \cos \theta_s - Q_n^0 \cos \theta_n}{\Delta \theta} \right\} + \frac{\Delta t}{2r \cos \theta_P} \left\{ \frac{Q_w^{1*} - Q_e^{1*}}{\Delta \phi} + \frac{Q_s^{1*} \cos \theta_s - Q_n^{1*} \cos \theta_n}{\Delta \theta} \right\} + (\dot{b}_s^0 + \dot{b}_{sb}^0 + d_{san}^0) \frac{\Delta t}{2} \quad (\text{B.12})$$

Leapfrog-Trapezoidal Scheme

Leapfrog (predictor) scheme

$$w_P^{(m+1)*} = w_P^{m-1} + \frac{2\Delta t}{r \cos \theta_P} \left\{ \frac{Q_w^m - Q_e^m}{\Delta \phi} + \frac{Q_s^m \cos \theta_s - Q_n^m \cos \theta_n}{\Delta \theta} \right\} + 2(\dot{b}_s^0 + \dot{b}_{sb}^0 + d_{san}^0) \Delta t \quad (\text{B.13})$$

Trapezoidal (corrector) scheme

$$\begin{aligned}
 w_P^{m+1} = & w_P^m + \frac{\Delta t}{2r \cos \theta_P} \left\{ \frac{Q_w^m - Q_e^m}{\Delta \phi} + \frac{Q_s^m \cos \theta_s - Q_n^m \cos \theta_n}{\Delta \theta} \right\} \\
 & + \frac{\Delta t}{2r \cos \theta_P} \left\{ \frac{Q_w^{(m+1)*} - Q_e^{(m+1)*}}{\Delta \phi} + \frac{Q_s^{(m+1)*} \cos \theta_s - Q_n^{(m+1)*} \cos \theta_n}{\Delta \theta} \right\} \\
 & + (b_s^0 + b_{sb}^0 + d_{san}^0) \Delta t
 \end{aligned} \tag{B.14}$$

B.4 The Darcy Water Flux Equation

Water flux at the western edge of grid cell

$$\begin{aligned}
 Q_w = & \left(\frac{2K_W K_P}{K_W + K_P} \right) \left(\frac{1}{\rho_w g r \cos(\theta_P) \Delta \phi} \right) \left[\right. \\
 & \max\{w_W[P_W - P_P + \rho_w g(z_{bW} - z_{bP})], 0\} \\
 & \left. - \max\{-w_P[P_W - P_P + \rho_w g(z_{bW} - z_{bP})], 0\} \right]
 \end{aligned} \tag{B.15}$$

Water flux at the eastern edge of grid cell

$$\begin{aligned}
 Q_e = & \left(\frac{2K_E K_P}{K_E + K_P} \right) \left(\frac{1}{\rho_w g r \cos(\theta_P) \Delta \phi} \right) \left[\right. \\
 & - \max\{w_E[P_E - P_P + \rho_w g(z_{bE} - z_{bP})], 0\} \\
 & \left. + \max\{-w_P[P_E - P_P + \rho_w g(z_{bE} - z_{bP})], 0\} \right]
 \end{aligned} \tag{B.16}$$

Water flux at the southern edge of grid cell

$$\begin{aligned}
 Q_s = & \left(\frac{2K_S K_P}{K_S + K_P} \right) \left(\frac{1}{\rho_w g r \Delta \theta} \right) \left[\right. \\
 & \max\{w_S[P_S - P_P + \rho_w g(z_{bS} - z_{bP})], 0\} \\
 & \left. - \max\{-w_P[P_S - P_P + \rho_w g(z_{bS} - z_{bP})], 0\} \right]
 \end{aligned} \tag{B.17}$$

Water flux at the northern edge of grid cell

$$Q_n = \left(\frac{2K_N K_P}{K_N + K_P} \right) \left(\frac{1}{\rho_w g r \Delta \theta} \right) \left[\begin{aligned} & - \max\{w_N [P_N - P_P + \rho_w g (z_{b_N} - z_{b_P})], 0\} \\ & + \max\{-w_P [P_N - P_P + \rho_w g (z_{b_N} - z_{b_P})], 0\} \end{aligned} \right] \quad (\text{B.18})$$

B.5 Hydraulic Conductivity

Hydraulic conductivity defined at cell centre

$$\log(K_P) = \frac{1}{\pi} (\log[K_{max}] - \log[K_{min}]) \tan^{-1} \left[k_a \left(\frac{w_P}{h_c} - k_b \right) \right] + \frac{1}{2} (\log[K_{max}] + \log[K_{min}]) \quad (\text{B.19})$$

B.6 Basal Water Pressure

Basal water pressure defined at cell centre

$$P_P = P_{I_P} \left(\frac{w}{h_c} \right)^{7/2} \quad (\text{B.20})$$

B.7 Condition for Tunnel Formation

$$|\vec{Q}| < \frac{|\vec{u}_0| Z_h}{(\rho_i L)^{-1} (\alpha - 1) \nabla (P + \rho_w g z)} \quad (\text{B.21})$$

When one of the Darcy flux equations exceeds the expression on the right hand side then water flow is considered to be channelized and is solved using the tunnel solver from Tarasov and Peltier (2006).

